

Prediction of Ka-band Radar Cross Section with THz Scale Models with Varying Surface Roughness

A thesis submitted in partial fulfillment
of the requirements for the degree of
Master of Science in Electrical Engineering

by

ANDREW J. HUEBNER
B.S.E.E., Wright State University, 2021

2023
Wright State University

Wright State University
College of Graduate Programs & Honors Studies

August 13, 2023

I HEREBY RECOMMEND THAT THE THESIS PREPARED UNDER MY SUPERVISION BY Andrew J. Huebner ENTITLED Prediction of Ka-band Radar Cross Section with THz Scale Models with Varying Surface Roughness BE ACCEPTED IN PARTIAL FULFILLMENT OF THE REQUIREMENTS FOR THE DEGREE OF Master of Science in Electrical Engineering.

Michael A. Saville, Ph.D., P.E.
Thesis Director

Michael A. Saville, Ph.D., P.E.
Chair, Department of Electrical Engineering

Committee on
Final Examination

Elliott R. Brown, Ph.D.

Yan Zhuang, Ph.D.

Shu Schiller, Ph.D.
Interim Dean, College of Graduate Programs & Honors Studies

ABSTRACT

Huebner, Andrew J. M.S.E.E., Department of Electrical Engineering, Wright State University, 2023.
Prediction of Ka-band Radar Cross Section with THz Scale Models with Varying Surface Roughness.

Radar cross section (RCS) of electrically large targets can be challenging and expensive to measure. The use of scale models to predict the RCS of such large targets saves time and reduces facility requirements. This study investigates Ka-band (27 to 29 GHz) RCS prediction from scale model measurements at 500 to 750 GHz. Firstly, the coherent quasi-monostatic turntable RCS measurement system is demonstrated. Secondly, three aluminum 18:1 scale dihedrals with surface roughness up to 218 microinches are measured to investigate how the roughness affects the Ka-band prediction. The measurements are compared to a parametric scattering model for the specular response, and indicate that the models' surface roughness have negligible effect on the RCS prediction.

Prediction of Ka-band Radar Cross Section with THz Scale Models with Varying Surface Roughness

Contents

1	Introduction	1
1.1	Motivation	1
1.2	Challenges	2
1.3	Research Hypothesis	2
1.4	Outline of Thesis	3
2	Background	4
2.1	THz Imaging Systems	4
2.2	THz Scattering from Rough Surfaces	12
2.3	Scale Model Measurements	14
2.4	Summary	16
3	Methodology	17
3.1	Introduction	17
3.2	THz Measurement System	17
3.2.1	Introduction	17
3.2.2	VDI Extension Modules & Antennas	18
3.2.3	Keysight N5224A	21
3.2.4	Newport Controller & Rotation Stage	22
3.2.5	MATLAB Control Software	23
3.2.6	Overall Design	24
3.3	Measurement Calibration	24
3.3.1	Calibration Assumptions	25
3.3.2	Calibration by a Reference Target	25
3.3.3	Background Subtraction	29
3.3.4	Range Gating	31
3.4	Scale Model Surface Roughness Experiment	33
3.4.1	Experiment Overview	33
3.4.2	Dihedral Targets	33
3.4.3	Experiment Parameters	35
3.4.4	Parametric Scattering Model	37
3.5	Analysis Method	38

4	Results	40
4.1	Introduction	40
4.1.1	A Note on Accuracy	40
4.2	THz Measurement System Performance	41
4.2.1	3-Inch Sphere RCS	41
4.2.2	ISAR Imaging	42
4.3	THz Dihedral Measurement Results	44
4.4	Ka-band Dihedral Measurement Results	53
4.5	Comparison of Scale Model Prediction to PM	55
4.6	Comparison of Scale Model Prediction to Ka-band Measurement	64
5	Conclusion	71
5.1	Summary	71
5.2	Recommendations for future work	72
	Bibliography	74

List of Figures

2.1	Schematic of a laser based terahertz transceiver at STL.	5
2.2	STL 1.5 THz imaging results.	6
2.3	JPL 675 GHz radar block diagram.	7
2.4	JPL radar image of person with PVC pipe.	8
2.5	Mostajeran et al. 220 GHz radar system.	9
2.6	Mostajeran et al. 220 GHz radar system images.	10
2.7	WSU scalar THz measurement system block diagram.	11
2.8	WSU scalar THz measurement Setup.	11
2.9	WSU ISAR image of 2-inch diameter mirror.	12
2.10	Diffuse scattering measuring setup.	13
2.11	An illustration of normalized scattering distribution caused by a slightly rough surface (red) and a rough surface (black) compared to the reflection by a smooth surface (blue) at a central frequency of 300 GHz.	14
3.1	VDI TxRef block diagram.	19
3.2	VDI Rx block diagram.	19
3.3	VDI modules mounted in a VV polarization with Thomas Keating corrugated horn antennas.	20
3.4	VDI modules with laser boresight aligner attached to lower antenna.	20
3.5	Keysight N5224A (option 400) block diagram.	21
3.6	Newport URS50BPP rotation stage in a leveling frame and with a keyed disc. The keyed plexiglass disc is paried with the styrofoam pedestal.	22
3.7	Target pallet resting on rotation stage with reflectors in the shape of a letter "A".	22
3.8	Target pedestal with a 3-inch square corner reflector resting on top	23
3.9	THz measurement system block diagram.	24
3.10	Range domain results of reference calibration	28
3.11	Frequency domain results of reference calibration	28
3.12	3-inch sphere measurement setup.	29
3.13	Range domain results of background subtraction.	30
3.14	Frequency domain results of background subtraction.	30
3.15	Range domain range gate comparison.	32
3.16	Frequency domain results of range gating	32

3.17	Dihedral geometry.	34
3.18	Scale model dihedral mounted on foam pedestal.	36
3.19	Ka-band dihedral mounted on foam pedestal.	37
4.1	Range profile for 3-inch sphere.	41
4.2	Measured RCS of 3-inch sphere.	42
4.3	ISAR measurement for letter “A”.	43
4.4	Experiment geometry for “A” measurement.	43
4.5	“A” ISAR image.	44
4.6	Polished scale model dihedral results at 600 GHz.	45
4.7	Normal scale model dihedral results at 600 GHz.	45
4.8	Rough scale model dihedral results at 600 GHz.	46
4.9	Polished scale model dihedral results at 625 GHz.	46
4.10	Normal scale model dihedral results at 625 GHz.	47
4.11	Rough scale model dihedral results at 625 GHz.	47
4.12	Polished scale model dihedral results at 650 GHz.	48
4.13	Normal scale model dihedral results at 650 GHz.	48
4.14	Rough scale model dihedral results at 650 GHz.	49
4.15	Polished scale model error.	50
4.16	Polished scale model relative error.	50
4.17	Machined scale model error.	51
4.18	Machined scale model relative error.	51
4.19	Rough scale model error.	52
4.20	Rough scale model relative error.	52
4.21	Ka-band dihedral results at 33 GHz.	54
4.22	Ka-band dihedral results at 34.375 GHz.	54
4.23	Ka-band dihedral results at 35.752 GHz.	55
4.24	Polished scale model prediction results at 33 GHz.	56
4.25	Normal scale model prediction results at 33 GHz.	56
4.26	Rough scale model prediction results at 33 GHz.	57
4.27	Polished scale model prediction results at 34.375 GHz.	57
4.28	Normal scale model prediction results at 34.375 GHz.	58
4.29	Rough scale model prediction results at 34.375 GHz.	58
4.30	Polished scale model prediction results at 35.752 GHz.	59
4.31	Normal scale model prediction results at 35.752 GHz.	59
4.32	Rough scale model prediction results at 35.752 GHz.	60
4.33	Polished scale model prediction error.	61
4.34	Polished scale model prediction relative error.	61
4.35	Machined scale model prediction error.	62
4.36	Machined scale model prediction relative error.	62
4.37	Rough scale model prediction error.	63
4.38	Rough scale model prediction relative error.	63
4.39	Error between polished model prediction and Ka-band measurement.	65
4.40	Relative error between polished model prediction and Ka-band measurement.	66
4.41	Error between machined model prediction and Ka-band measurement.	67

4.42	Error between machined model prediction and Ka-band measurement.	68
4.43	Error between rough model prediction and Ka-band measurement.	69
4.44	Error between rough model prediction and Ka-band measurement.	70

List of Tables

3.1	Major Components of THz System	18
3.2	3-inch sphere experiment parameters	27
3.3	Dihedral Manufacturing Specifications	33
3.4	Dihedral surface roughness	34
3.5	Scale Model Measurement Specifications	35
3.6	Ka-band Measurement Specifications	36
4.1	ISAR Experiment Parameters	42
4.2	Scale Model Error	53
4.3	Error Between Prediction and PM	64
4.4	Error Between Prediction and Measurement	70

Acknowledgment

There are more people than I could possibly acknowledge here. I owe much thanks to my family, especially my parents, for supporting and encouraging me throughout my education. I truly could not have done it without them. I am thankful for the guidance of Dr. Michael Saville, who took me on as an undergrad researcher and later as my thesis advisor. Dr. Elliott Brown provided excellent guidance, expertise and encouragement for this work. I also want to recognize all of my fellow students and SSEL researchers. Their support and friendship helped me keep going.

“To the King of ages, immortal, invisible, the only God, be honor and glory forever and ever. Amen.”

Dedicated to
Bob Drummond
U.S. Army Radio Technician
Husband, Father, Grandfather
Servant of Christ

Introduction

1.1 Motivation

Scale models are used to predict the scattering behaviors of full-size targets. Full-size targets of interest may be expensive, challenging, or practically impossible to obtain and measure. Besides simulations, scale model measurements offer an opportunity to estimate the scattering of these targets without actually measuring the object itself.

In order to produce accurate predictions via scale model measurements, it must be ensured that the model is congruent with the target. If a target is not modeled properly then inaccurate predictions will be made. One parameter of interest is surface roughness. To what degree must the surface roughness of a target be taken into account when making a scale model? While the surface roughness may be insignificant to a full-size target RCS measurement, at higher frequencies used to measure the scale models the same surface roughness could lead to different scattering behavior leading to error in the RCS prediction.

The motivation of this paper is to investigate the effects of varying the surface roughness of scale models used to predict the radar cross section (RCS) of a Ka-band target.

1.2 Challenges

One major challenge in this investigation is the lack of an accessible measurement system operating in the THz region. THz measurement systems are not widely used or common. To perform this investigation a THz measurement system must first be developed which is capable of performing the measurements of scale models. In the first part of this work, a coherent radar system is assembled and demonstrated for operation at 500-750 GHz, i.e. in the lower spectrum of the THz band (300 GHz to 3,000 GHz).

1.3 Research Hypothesis

An experiment is designed to investigate the effects of varying surface roughness on scale model measurements. Four aluminium dihedrals are machined, one dihedral is designed for Ka-band measurements and three THz scale models are made with varying roughness. One sample is as machined using standard end mill cutting, one is hand-polished using a Scotch Bright pad, and one is bead blasted using heavy grit via air pressure. The goal of the experiment is to determine whether or not polishing the standard milled sample is required to accurately model the Ka-band target. Polishing scale models adds time and financial costs that could otherwise be avoided. If standard end mill cutting is sufficient then both lead time and cost to create these scale models could be reduced. The bead blasted sample is tested to determine if the increased roughness results in any noticeable effect. The experiment hypothesis is that the polished sample will produce the most accurate Ka-band target RCS prediction, followed by the standard milled sample and lastly the bead blasted sample. The experiment will investigate this hypothesis by quantifying the error between the scale model prediction and the Ka-band target. Results will be examined in two ways: 1) comparison of each sample RCS to that of a parametric scattering model prediction 2) comparison of the scale model RCS prediction to the full size target RCS.

1.4 Outline of Thesis

In Chapter 2 an overview of research in the areas of THz measurement systems and THz rough surface scattering is presented. An overview of scale-model RCS prediction is presented along with an example of a real world application. In Chapter 3 the THz measurement system is described, the RCS measurement process is described and demonstrated, and the scale model experiment is explained along with the method used to analyze the results. Chapter 4 provides the experiment results with descriptions. Chapter 5 provides an over view of the results, how the results support or oppose the hypothesis, and recommendations for future work.

Background

2.1 THz Imaging Systems

Terahertz technology is a broad area of interest in the field of radar imaging. Some specific areas of application include medical imaging [1], concealed object detection [2], degraded visibility environment imaging [3], and target signature measurement and prediction [4]. Because of the high frequency and short wavelength compared to more common radar bands, such as X-band (8-12 GHz) or Ka-band (27-40 GHz), terahertz radar systems can be built in a smaller form factor while achieving high directivity and small beam spot size. The shorter wavelength can allow for the resolution of features not observable by traditional imaging radar and provides the opportunity to investigate material properties at these higher frequencies [5]. Over the years, THz measurement systems have been built using various transmitter and receiver designs, various imaging methods, and for many applications. The rest of this section will provide a brief overview of some of these systems as well as their application and some results.

The Submillimeter Wave Technology Laboratory (STL) at UMass Lowell has been developing submillimeter and THz measurement systems for over twenty years and have published many papers demonstrating the design and capabilities of these systems [6, 7, 4, 8, 9, 10]. Some systems have been built using optically pumped, molecular gas lasers, which were more capable of providing the power desired for their measurements than solid state technology at the time [6, 11]. These system may require the careful set up of mirrors,

lenses and beam splitters. Some more recent systems use phase-locked loop (PLL) synthesizers and frequency multipliers to construct the transmit and receive modules without requiring lasers or quasi-optical components [10]. The STL has used both of these system types to produce impressive measurements including RCS range profiles, range-Doppler maps of moving targets [10] and high resolution images [11] as well as the use of scale models to predict the scattering of larger targets at lower frequency bands.

Figure 2.1 shows a schematic of a typical laser based THz imaging system at STL from 2004 described in [11]. This system uses two CO₂ far-infrared (FIR) lasers to generate a transmit signal and LO signal at 1.5645 THz and 1.5626 THz, respectively. The transmitter/receiver component sits just outside of the anechoic chamber, which uses physical geometry and THz absorber material to reduce unwanted scattering. A set of optical mirrors and a focusing mirror are used to direct the transmit beam and provide a planar phase front with a 24-inch full-width-half-maximum (FWHM) that fully illuminates the target. The backscattered signal is similarly directed to Schottky diode receivers for both vertical and horizontal polarization. A lock-in amplifier is used to recover the complex target response.

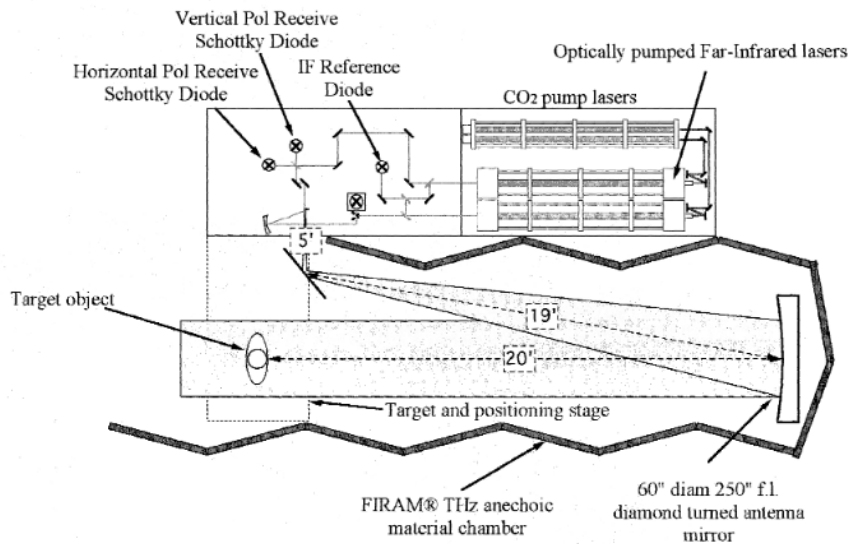


Figure 2.1: Schematic of a laser based terahertz transceiver at STL. [11]

In this system, measurements are taken at a single frequency while the azimuth and elevation angle are varied in a uniform pattern. Change in the azimuth of the target provides phase history which can resolve the target signature in the horizontal dimension, while change in the elevation angle of the target provides phase history which can resolve the vertical signature of the target. By use of a 2D Fourier Transform, a 2D image of the target is generated. Figure 2.2 shows the results of imaging a 1/16 scale model truck with 1.1 mm square pixels. The top image is computed from the THz measurement data and the bottom image is a photograph including an apple for scale.

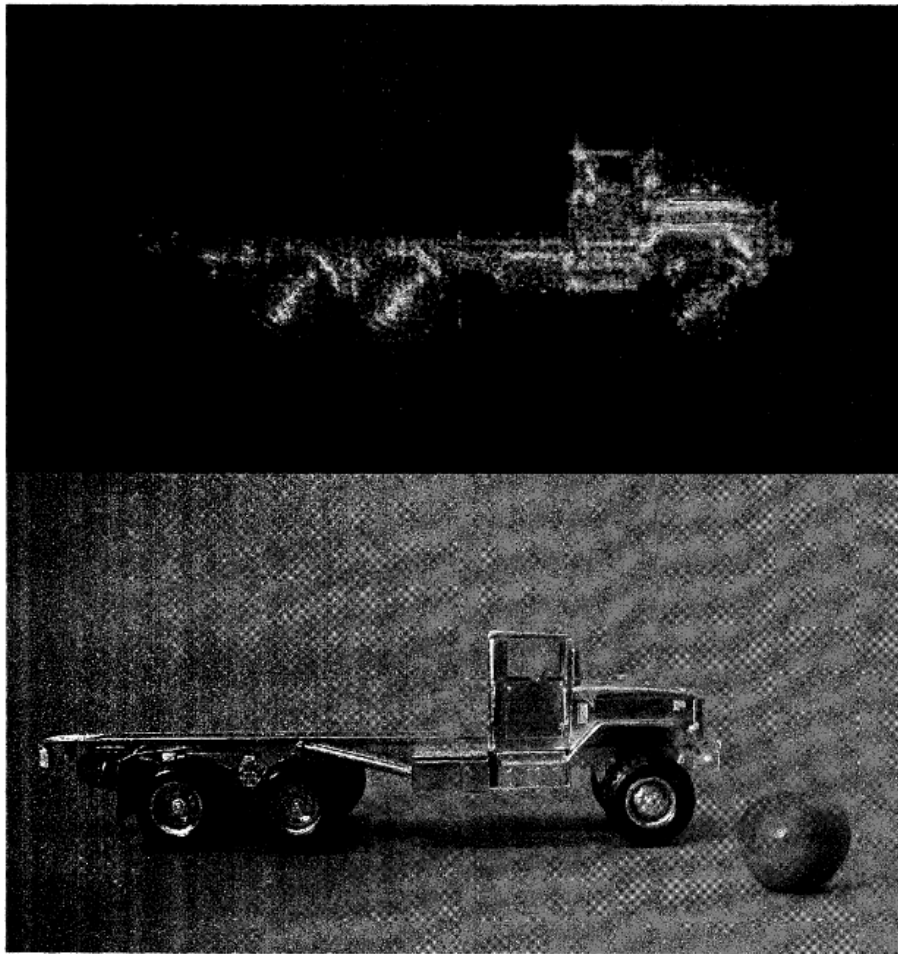


Figure 2.2: STL 1.5 THz imaging results. [11]

A 2018 paper published by STL describes a 243 GHz direct-conversion measurement system [10]. This system uses a PLL-based X-band synthesizer and frequency multiplier

to generate the transmitted signal and a second frequency multiplier and scalar homodyne receiver to recover the received signal. Short duration frequency sweeps are used to find the range and velocity of targets.

NASA's Jet Propulsion Laboratory (JPL) has been developing THz measurement systems for applications including concealed object detection [12] [13] [14]. In 2011 JPL published a description of a prototype 675 GHz imaging system with the ability to identify concealed objects on people through clothing [15]. This system uses a Ka-band source generator and frequency multipliers to produce a 676.7 GHz frequency-modulated continuous-wave (FMCW) signal with a 28.8 GHz bandwidth and a coherent receiver unit records the complex target response. Figure 2.3 shows the block diagram of the system.

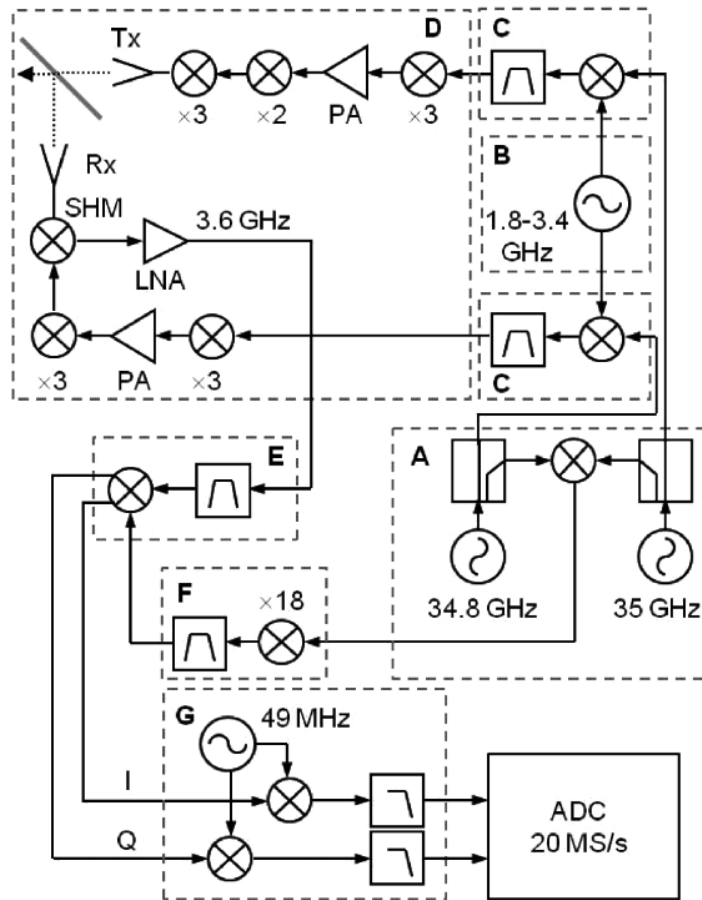


Figure 2.3: JPL 675 GHz radar block diagram. [15]

An optical system including a 1 meter diameter aperture focuses the transmitted signal into a 1-cm spot size at a range of 25 meters. By rotating a mirror, a square area of 40x40 cm can be measured at one frame per second. Figure 2.4 shows the generated image for a person with a PVC pipe attached to them. This image was generated in one second and the pipe is clearly visible.

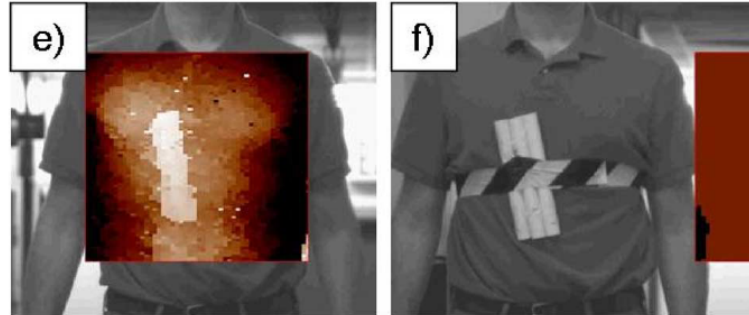


Figure 2.4: JPL radar image of person with PVC pipe. e) radar image overlaid on photograph f) photograph of target area. [15]

A 2018 paper by Mostajeran et al. demonstrates a 220 GHz fully integrated imaging radar [16]. The transceiver unit is compact (less than one square centimeter) and uses a FMCW signal with 62.4 GHz of bandwidth. Using inverse synthetic aperture radar (ISAR) imaging techniques, a lateral range resolution of 2 mm and a range resolution of 2.7 mm is achieved for a target at a distance of 23 cm. Figure 2.5 shows the block diagram of the system and the die micrograph.

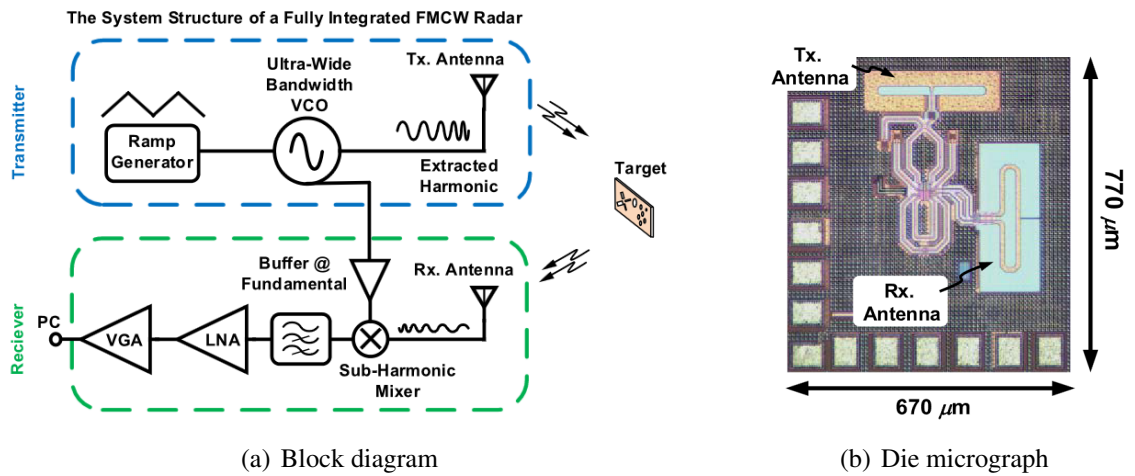


Figure 2.5: Mostajeran et al. 220 GHz radar system. [16]

The system is mounted on a PCB and positioned across from the target, which is translated in position laterally and vertically. 2D and 3D images of the target can be generated from the collected data. Figure 2.6 shows a test target and the generated images.

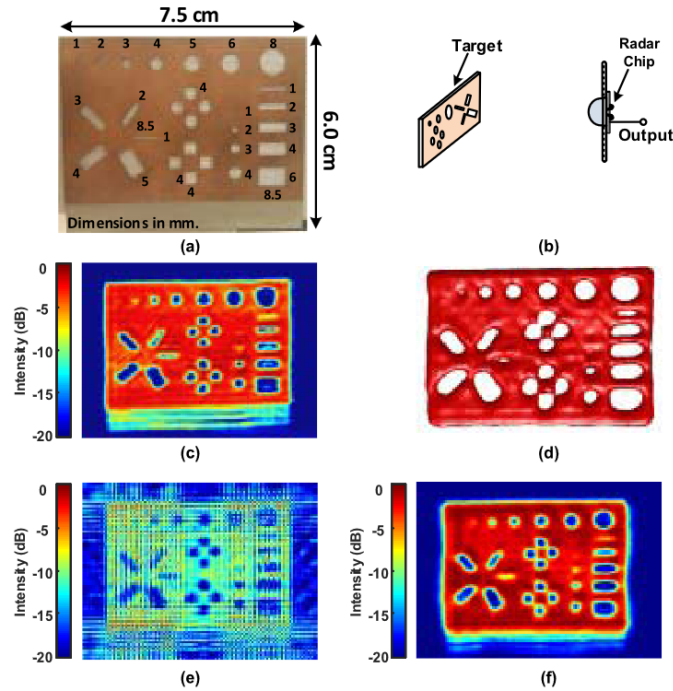


Figure 2.6: Mostajeran et al. (a) Stencil reflector as a benchmark for imaging. (b) Plane wave imaging setup. (c) Experimental results of ISAR image of the stencil at 15 cm from the radar with a spatial sampling distance of 1 mm. (d) 3-D image of the scene from the reconstructed volume. (e) Reconstructed ISAR image for a spatial sampling distance of 2 mm to demonstrate the effect of the grating lobes. (f) Experimental results of ISAR image of the stencil at a distance of 23 cm. [16]

The Signals and Sensors Exploitation Lab (SSEL) and THz Sensors Group at Wright State University (WSU) are developing THz imaging capabilities and published a paper in 2022 describing an initial system [17]. This system operates at a center frequency of 600 GHz with 40 GHz of available bandwidth. An Anritsu MG3692C signal generator is used to generate signals in the 12-13 GHz range which are then passed through a 48x multiplier chain to produce the desired transmit signal, which is propagated towards the target via an open ended waveguide antenna. A thermal receiver unit, later replaced with a rectifier detector, sits in a bistatic configuration and receives the bistatic scattering which is then recovered with a Stanford Research Systems SR830 DSP lock-in amplifier as amplitude only. A signal generator is used to amplitude modulate the transmitted signal and provide the reference for the lock-in. Figure 2.7 shows the block diagram of this system, figure 2.8

show an experiment setup to measure a 2-inch diameter mirror with annotations and figure 2.9 shows the ISAR image of the mirror.

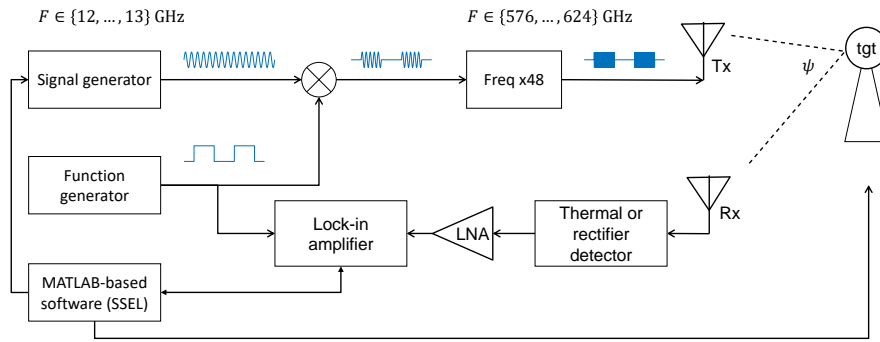


Figure 2.7: WSU scalar THz measurement system block diagram. [17]

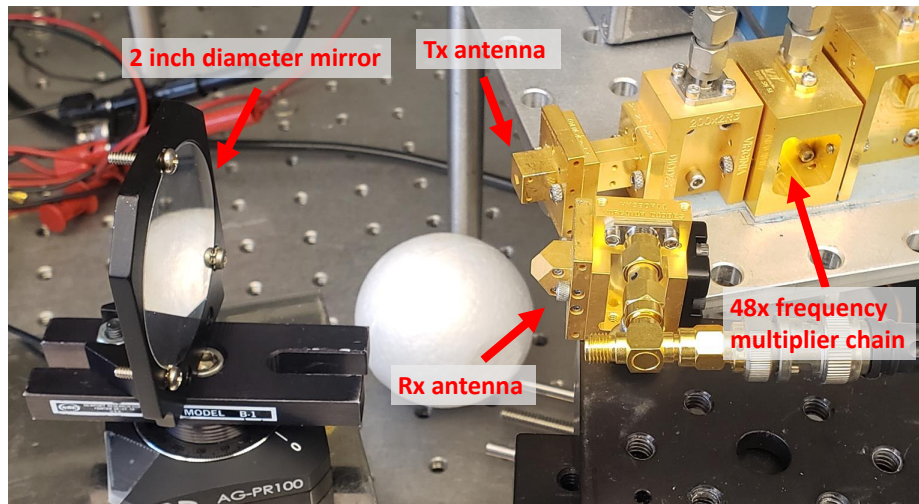


Figure 2.8: WSU scalar THz measurement Setup. [17]

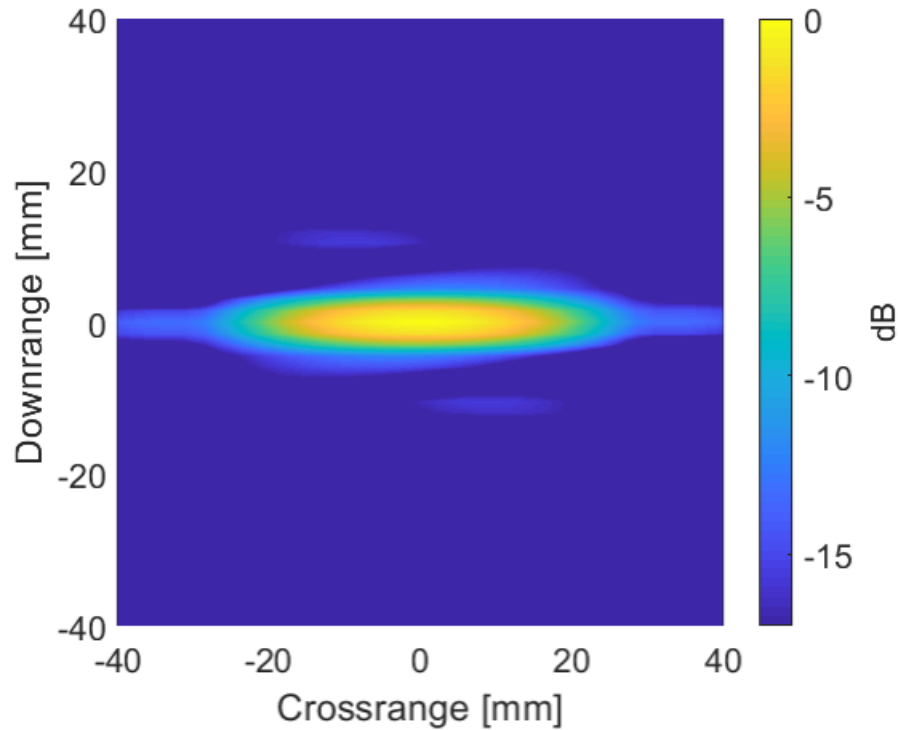


Figure 2.9: WSU ISAR image of 2-inch diameter mirror. [17]

Limitations of this system include long lock-in integration times (>300 mS) leading to long collection times, a large bistatic angle (~ 22 deg), a small target measurement area, and a lack of phase data. Targets more than two inches across are challenging to fully illuminate because the sensitivity does not allow the standoff range to be increased far enough to fully illuminate the target. A system created from commercially available parts that can quickly measure the complex THz scattering of targets at a farther standoff range with a smaller bistatic angle is desired.

2.2 THz Scattering from Rough Surfaces

There has been increased interest in the last decade in accurately measuring and estimating the scattering of materials with varying surface roughness at THz frequencies. The demand for more throughput is driving a shift to the increased bandwidth available at higher fre-

quency bands, and with this a greater understanding of the scattering at these frequencies is desired [18]. There is a specific interest in studying the diffuse scattering at these frequencies and how non-line-of-sight communication may be used [19]. This section will review some current research in the area of THz scattering from rough surfaces.

A 2016 study by Alissa et al. investigated the effects of varying surface roughness on THz scattering [20]. In this study, custom-made surfaces are produced via 3D printing. The height is normally distributed and the correlation length is controlled. Surfaces with varying height distribution variance and varying correlation length are produced.

Each surface is examined by measuring the coherent scattering over a range of reflection angles while illuminating the surface at a fixed incident angle. The system can perform scattering measurements from 100 GHz to 1.3 THz. Figure 2.10 shows the measurement setup.

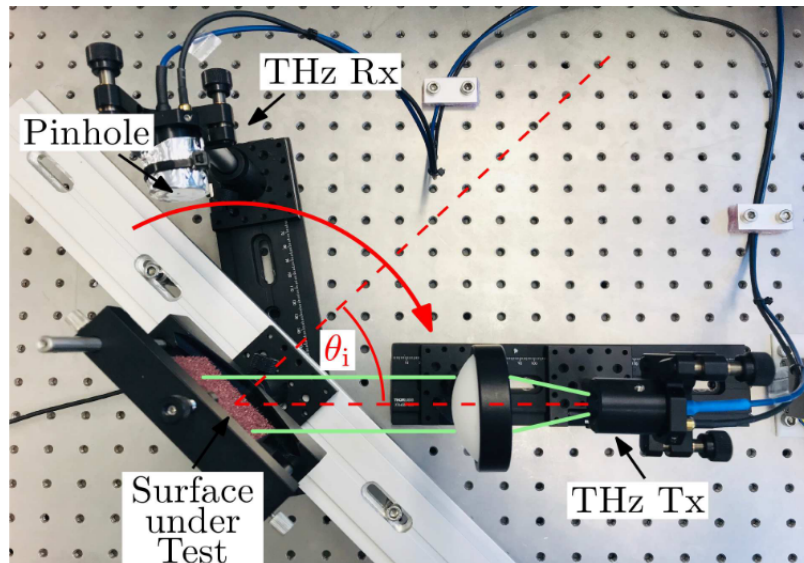


Figure 2.10: Diffuse scattering measuring setup. [20]

A set of measurements taken at 300 GHz demonstrate that for rougher surfaces the specular scattering is weaker and that increased surface roughness increases diffuse scattering, as shown in Figure 2.11.

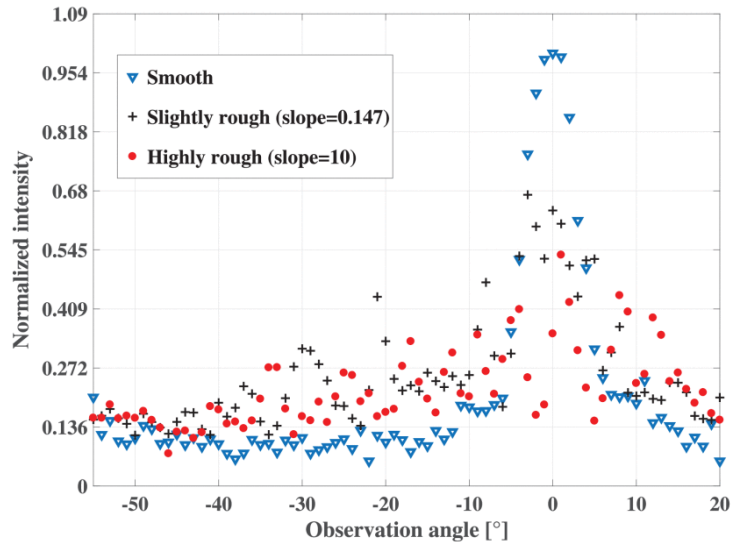


Figure 2.11: An illustration of normalized scattering distribution caused by a slightly rough surface (red) and a rough surface (black) compared to the reflection by a smooth surface (blue) at a central frequency of 300 GHz. [20]

2.3 Scale Model Measurements

Scale models measurements can be used to predict the scattering of full-size targets. For a scale model with scale factor s (where $s = 1/10$ for a model that is 1/10 the size of the normal size target), it can be shown via derivation from Maxwell's equations that the measurement frequency should be scaled as

$$f_2 = \frac{1}{s} f_1, \quad (2.1)$$

where f_1 and f_2 represent the full-size target measurement frequency and scale model measurement frequency, respectively [21]. This condition ensures that the scale model target is the same electrical size in terms of wavelength as the full-size target. It can further be shown that the theoretical RCS of the scale-model target is proportional to the RCS of the

full-size target times the square of the scale factor as show in (2.2) [21].

$$\text{RCS}_2 = s^2 \text{RCS}_1 \quad (2.2)$$

The RCS of a full-size target can therefore be predicted by use of a scale model with scale factor s , measured at the frequency determined via (2.1), as

$$\text{RCS}_1 = \frac{1}{s^2} \text{RCS}_2. \quad (2.3)$$

It is important to note that the use of (2.2) in predicting the RCS of targets is only valid when the scale model meets certain conditions that may be challenging or even impossible for certain targets. In addition to, scaling the measurement frequency, the material properties of the scale model must also be scaled if the same scattering behavior is to be observed. There are two conditions that must be met. First, the complex wavenumber of the material at the scaled frequency must match that of the full size target at its measurement frequency [21].

$$k_2 = \omega_2 \sqrt{\mu_2 \epsilon_2} = \frac{k_1}{s}. \quad (2.4)$$

And second, the intrinsic impedance of the scale model must match that of the full size target [21].

$$Z_2 = Z_1. \quad (2.5)$$

For dielectric and absorbing materials, then, the materials themselves must have properties that behave at the scaled frequency as they would at the normal target measurement frequency. Scale models cannot simply be made using the same materials as the real target and accurate predictions be expected. When using strictly highly conductive, metallic material these constraints are satisfied.

Scale models are used in practice for various applications. In [22], scale model mea-

measurements are demonstrated for the application of predicting interference caused by the presence of wind turbines in the area of a radar system. Scale models with a scale factor of 1/100 are used to predict full-size wind turbine scattering at varying angles and blade rotation velocity.

2.4 Summary

THz measurement technology has been developing for decades and continues to be an area of interest with applications in imaging and object detection. Laboratory measurement systems are capable of generating ISAR images of targets using commercially accessible components and without the need for large controlled test environments. The effects of surface roughness on THz scattering is being actively investigated and it has been experimentally demonstrated that rougher surfaces reduce the peak specular scattering and increase diffuse scattering. Scale models can be used to accurately predict the scattering of full-size targets if measured under appropriate conditions and are used in practice today.

Methodology

3.1 Introduction

In this chapter, the methodology of the research will be explained. As stated in Chapter 1, the purpose of this work is to determine the effects of surface roughness when using scale model targets at THz to predict the scattering of a full-size target at Ka-band. This chapter will describe the measurement system used to take the measurements of the scale models, the experiment designed to investigate the hypothesis, and how the results will be calculated and presented.

3.2 THz Measurement System

3.2.1 Introduction

This section describes the instrumentation setup and data collection procedure used to collect data for this research, as well as how data is processed and how experiment results are quantified and interpreted. Terahertz scattering data is collected in the Wright State University Sensors and Signals Exploitation Lab (SSEL) via an in-house measurement system consisting of a VNA, transmit and receive frequency extenders, and a controllable motorized target mount. The SSEL has previously published papers in the area of inverse synthetic aperture radar measurements for the application of automatic target recognition

[23], [24], and RCS measurements in partially controlled environments [25]. The measurement system in this paper is integrated into existing SSEL capabilities with additional hardware and software as needed.

The THz measurement system was developed using commercially available equipment. Table 3.1 lists the major components of the THz system. The rest of this section describes the overall system design as well as the individual components and what role each plays in the system.

Table 3.1: Major Components of THz System

Device	Manufacturer	Model Number
PNA	Keysight [26]	N5224A
TxRef Frequency Extender	VDI [27]	VNAX TxRef
Rx Frequency Extender	VDI [27]	VNAX Rx
Coaxial Amplifier	MiniCircuits [28]	ZKL-1R5
Motion Controller	Newport [29]	ESP301
Rotation Stage	Newport [30]	URS50BPP
Diagonal Horn Antenna	VDI	WR1.5 diagonal horn
Corrugated Horn Antenna	Thomas Keating [31]	N/A

3.2.2 VDI Extension Modules & Antennas

The TxRef and Rx modules manufactured by Virginia Diodes, Inc. (VDI) are coherent frequency extenders that allow for transmitting and receiving signals from 500 to 750 GHz. The modules contain 54x frequency multipliers which make it possible to generate these higher frequencies using signals in the 9 to 14 GHz frequency range, well within the capabilities of a microwave network analyzer such as the N5224A with a operating range of 10 MHz to 43.5 GHz.

The TxRef module has two inputs and two outputs, as seen in the block diagram provided in Figure 3.1. The RF input is amplified, frequency multiplied by a factor of 54, and sent to the test port, which consists of a WR 1.5 waveguide with an attached VDI diagonal horn antenna. The second input, LO, is also frequency multiplied by a factor of 54 and is then mixed with the frequency multiplied RF input. The output of the mixer is

amplified and has a frequency of $54(f_{RF} \pm f_{LO})$. This mixed signal is referred to as the intermediate frequency of the transmitter module and is sent to the output named Reference (R, or “Ref.” in Fig. 3.1).

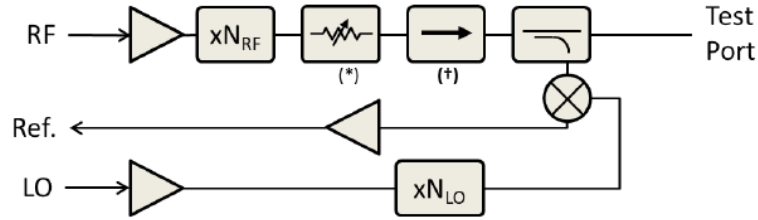


Figure 3.1: VDI TxRef block diagram. [32]

The Rx module has one input and two outputs, as seen in the block diagram provided in Figure 3.2. The test port consists of a WR 1.5 waveguide with an attached VDI diagonal horn antenna. This input is then mixed with the $54x$ frequency multiplied LO input signal, and the resulting signal is amplified and has a frequency of $54(f_{RF} \pm f_{LO})$. This mixed signal is referred to as the intermediate frequency of the receiver module and is sent to the output named Measure (M, or “Meas.” in Fig. 3.2).

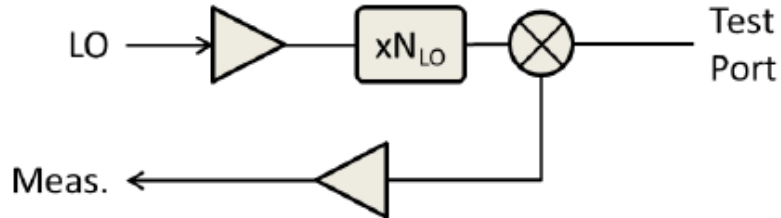


Figure 3.2: VDI Rx block diagram. [32]

When provided with the same LO input, a signal transmitted by the TxRef module and received by the Rx module will result in the two modules outputting an identical intermediate frequency. The output R is used as a reference signal to recover the signal M using a device such as a lock-in amplifier, or R can be used as a phase reference while measuring R and M with coherent receivers as in this research.

Two Thomas Keating corrugated horn antennas are used in a vertical polarization configuration. These antennas radiate a Gaussian beam with an approximately 8-degree half-power beamwidth at 600 GHz and a gain of 28 dBi. A custom sleeve with a laser boresight aligner is used to align each antenna to the proper spot. Figure 3.3 show the antennas attached to the VDI modules.

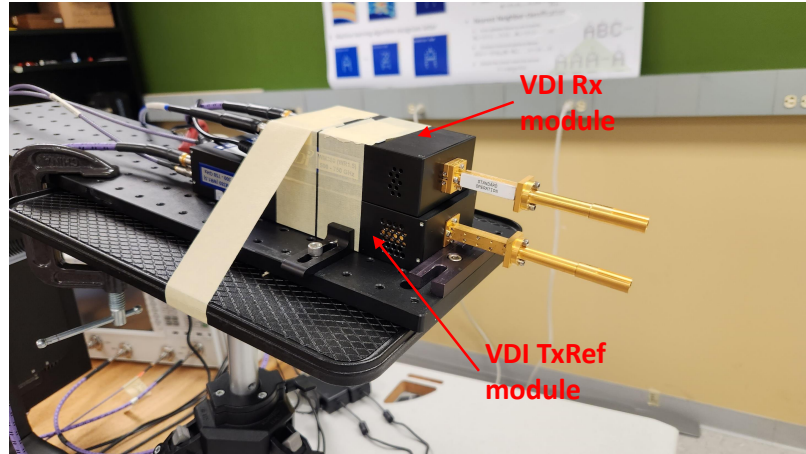


Figure 3.3: VDI modules mounted in a VV polarization with Thomas Keating corrugated horn antennas.

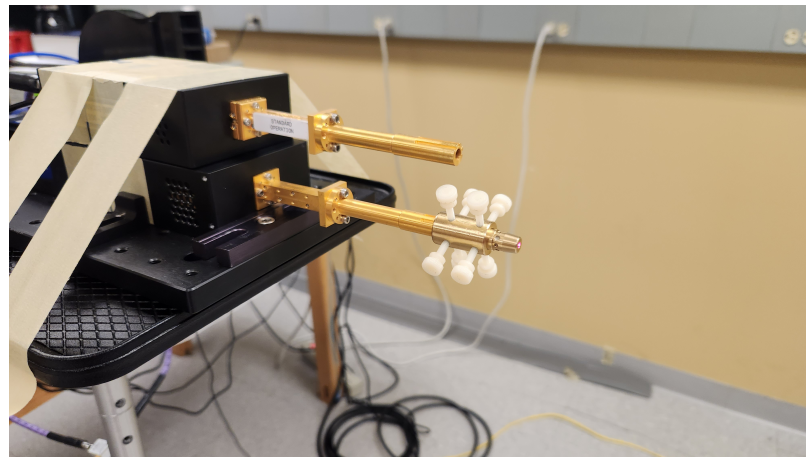


Figure 3.4: VDI modules with laser boresight aligner attached to lower antenna.

3.2.3 Keysight N5224A

A Keysight N5224A performance network analyzer is an essential component of the measurement system. The PNA is used to generate both the RF and LO signal inputs for the VDI modules as well as to measure both the R and M outputs of the modules. The operating range of the PNA (10 MHz to 43.5 GHz) allows for the full range of the VDI modules to be utilized. The N5224A provides two internal sources which can be set independently. Source 1 is used to generate the RF signal on Port 1 and Source 2 is used to generate the LO signal on Port 3. By taking advantage of the Frequency Offset Mode (FOM) of the PNA, the receiver reference frequencies can be set to any frequency within the devices operating range independently from the source frequencies. Using FOM allows the receiver frequencies to be set to the intermediate frequency of the VDI modules. Port 4 is used to measure the R output of the TxRef module and Port 2 is used to measure the M output of the Rx module. By using both sources, FOM, and directly accessing the receivers of Ports 4 and 2, the PNA is used to drive all of the inputs and record all of the outputs. Figure 3.5 shows a block diagram of the internal configuration of the N5224A with option 400.

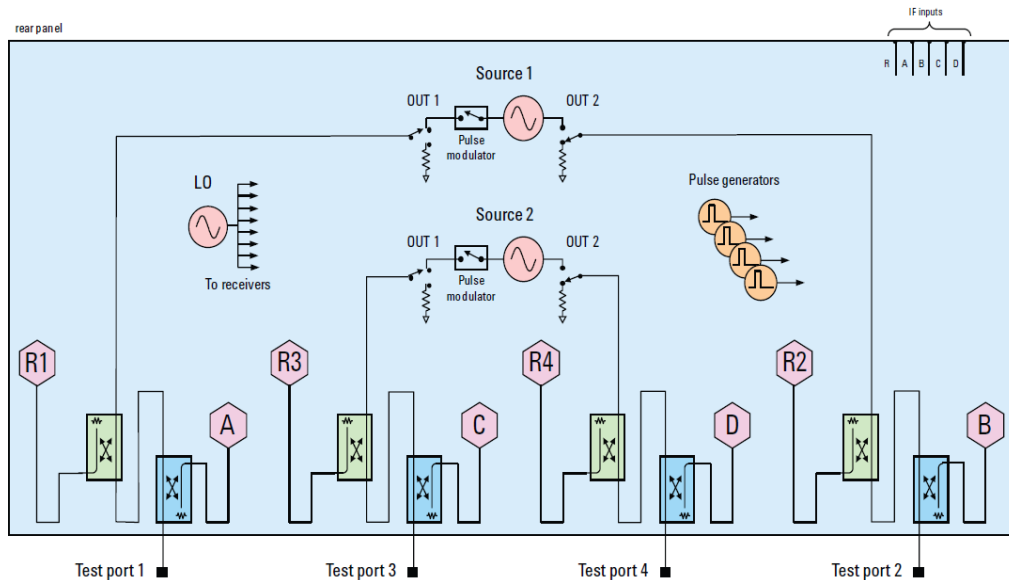


Figure 3.5: Keysight N5224A (option 400) block diagram. [33]

3.2.4 Newport Controller & Rotation Stage

A Newport ESP301 motion controller drives a Newport URS50BPP rotation stage which is embedded in a leveled mount resting on the floor. The mount allows for either a flat pallet or a styrofoam pedestal to be attached as a target support.

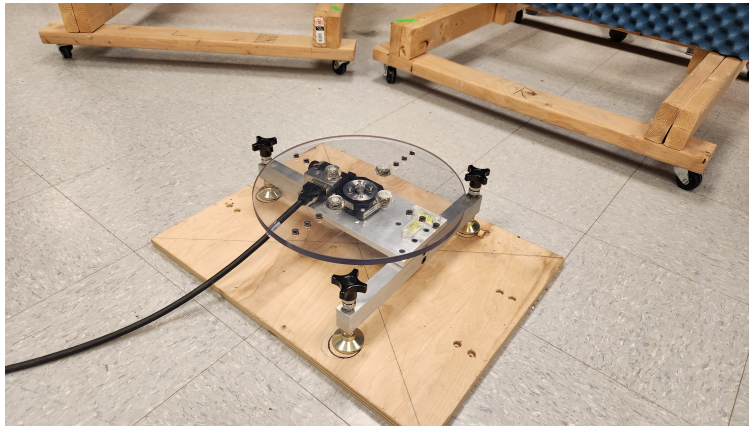


Figure 3.6: Newport URS50BPP rotation stage in a leveling frame and with a keyed disc. The keyed plexiglass disc is paired with the styrofoam pedestal.

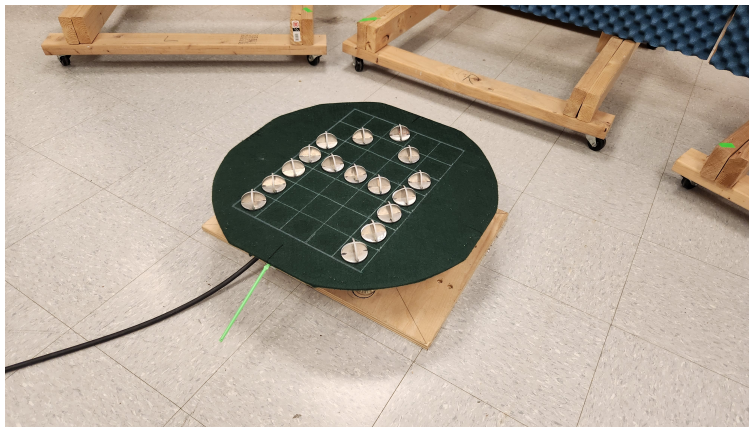


Figure 3.7: Target pallet resting on rotation stage with reflectors in the shape of a letter “A”.

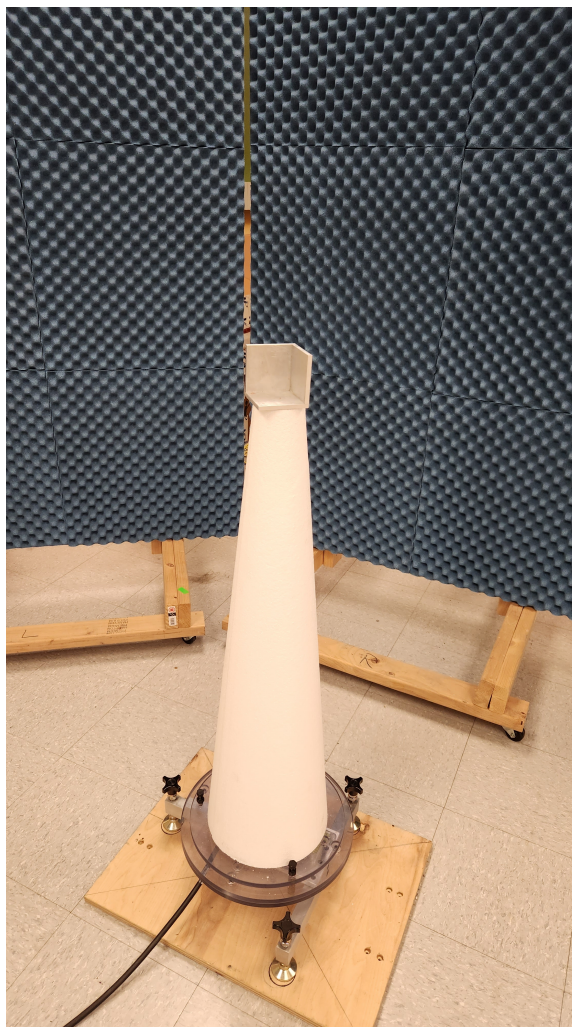


Figure 3.8: Target pedestal with a 3-inch square corner reflector resting on top

3.2.5 MATLAB Control Software

Custom MATLAB-based software has been developed by the SSEL for controlling instruments, querying measurement data, and processing the collected data. Experiment control scripts allow for automated data collection according to provided experiment parameters. Instrumentation is accomplished via USB serial communication for the motion controller and via a GPIB to USB adaptor for the PNA.

3.2.6 Overall Design

Figure 3.9 shows the block diagram of the entire system. The VDI TxRef and Rx modules act as the transmitter and receiver, respectively, while the PNA is used to both generate the input signals to the VDI modules and to record the reference signal from the TxRef module and the measured signal from the Rx module. The PNA calculates the ratio between M and R using the math function B/D. This quotient is displayed on the analyzer and is queried via MATLAB software.

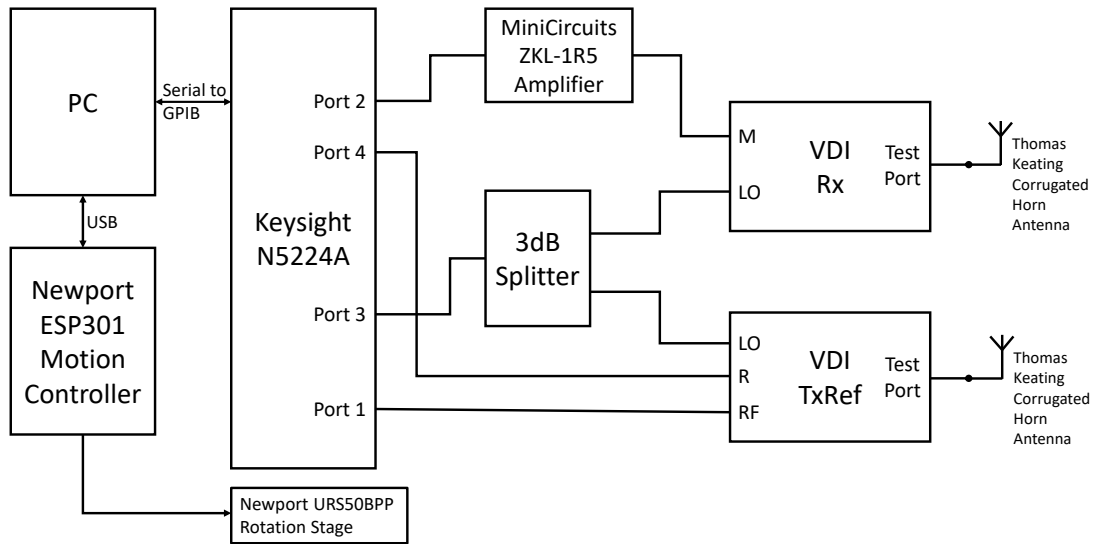


Figure 3.9: THz measurement system block diagram.

3.3 Measurement Calibration

Taking a single measurement of a target is not sufficient to produce high-quality RCS measurements or images. Scatter from the measurement environment can corrupt the RCS measurement and produce features in images that are not a result of the target. The lack of a uniform frequency response of the system also results in artifacts that corrupt the measurement. Three methods are used to address these issues: calibration by a reference target,

background subtraction and range gating.

In this section, measurement data for a 3-inch diameter conducting sphere is used to demonstrate these methods and provide an example using real measurement data taken with the measurement system. The theoretical RCS of a perfectly conducting sphere is calculated as

$$\sigma_{sphere} = \pi a^2, \quad (3.1)$$

where a is the radius of the sphere, leading to $\sigma_{thry} = -23.41$ dBsm for the three-inch sphere. This section follows IEEE Standard 1502-2020 for radar cross-section test procedures [34].

3.3.1 Calibration Assumptions

The RCS calculation and calibration techniques used in this project rely on several assumptions. First, it is assumed that the target is fully illuminated by a plane-wave. The antennas actually radiate a Gaussian beam and no technique is used to produce a plane-wave at the target. Second, it is assumed that the target is isolated and measured in open space. This is clearly not the case as the measurement setup in the lab is far from open-space. Walls, floor, ceiling, workstations, and other objects surround the measurement area. The target is also mounted on a styrofoam pedestal. Electromagnetic interactions between the target and the pedestal will alter the scattered response so that an isolated measurement is not measured. Therefore, the RCS calculation and calibration process does not perfectly account for this specific setup and the assumptions made could lead to errors in the final RCS results.

3.3.2 Calibration by a Reference Target

The measured scattering of a target can be represented as the response of a linear system as

$$E_m^t(f) = E_a^t(f)H(f), \quad (3.2)$$

where $E_m^t(f)$ is a complex number representing the magnitude and phase of the measured target response, $E_a^t(f)$ similarly represents the actual target response, and $H(f)$ is the complex frequency response of the system. All else being the same, the actual target response can be determined as

$$E_a^t(f) = \frac{E_m^t(f)}{H(f)}. \quad (3.3)$$

By dividing the measured target response by the measured response of a reference target with a known response a scaled target measurement can be calculated as

$$\frac{E_m^t(f)}{E_m^r(f)} = \frac{E_a^t(f)H(f)}{E_a^r(f)H(f)} = \frac{E_a^t(f)}{E_a^r(f)}. \quad (3.4)$$

Solving for the actual response of the target results in an equation where all of the variables are either known or measured, providing a process by which the actual target measurement can be calculated as

$$E_a^t(f) = \frac{E_m^t(f)}{E_m^r(f)} E_a^r(f). \quad (3.5)$$

By setting $|E_a^r(f)| = \sqrt{\sigma_r(f)}$, where $\sigma_r(f)$ is the RCS of the reference target, the target RCS is then calculated as the squared magnitude of (3.5) as

$$\sigma_t(f) = |E_a^t(f)|^2 = \left| \frac{E_m^t(f)}{E_m^r(f)} \right|^2 |E_a^r(f)|^2 = \left| \frac{E_m^t(f)}{E_m^r(f)} \right|^2 \sigma_r(f), \quad (3.6)$$

where $\sigma_t(f)$ is the calculated target RCS.

The calibrated frequency domain of the target provided by (3.5) may be transformed into the range domain using the Inverse Fourier Transform. In this case, the Inverse Fast Fourier Transform (IFFT) is used to transform the discrete samples in frequency to samples in range, where $s(m)$ shown below is the calibrated scattering response as a function of range.

$$s(m) = \mathcal{F}^{-1}\{E_a^t(f)\} \quad (3.7)$$

The RCS as a function of range can then be calculated as the squared magnitude of (3.7).

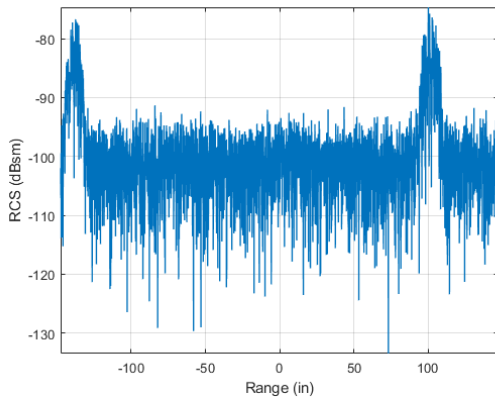
$$\sigma_t(m) = |s(m)|^2 \quad (3.8)$$

Table 3.2 lists the experiment collection parameters as well as the corresponding range resolution and unambiguous range, which are a function of the sampling parameters and described in [35].

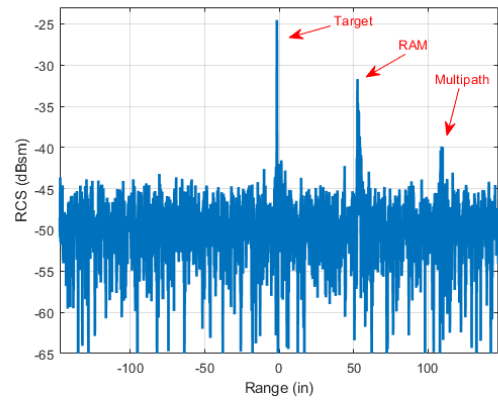
Table 3.2: 3-inch sphere experiment parameters

Parameter	Value
Center frequency	620 GHz
Bandwidth	40 GHz
Frequency step size	20 MHz
Range resolution	3.75 mm
Unambiguous range	7.5 m

Using a 6-inch diameter conducting sphere as the reference target, Figures 3.10 and 3.11 show the effects of reference target calibration via 3.5 and 3.6 on the RCS calculation of the 3-inch sphere in the range and frequency domains, respectively. In Figure 3.10, a significant change is noted. Three peaks occur which are more narrow than those before calibration. The calibration sets the range origin at the center of the cal target, and the range of the three peaks correspond to real scattering features which are identified and labeled. This calibration also corrects the magnitude scale. Figure 3.12 shows the experiment setup with annotations. In Figure 3.11 the main effect noted is that the magnitude accuracy is improved.

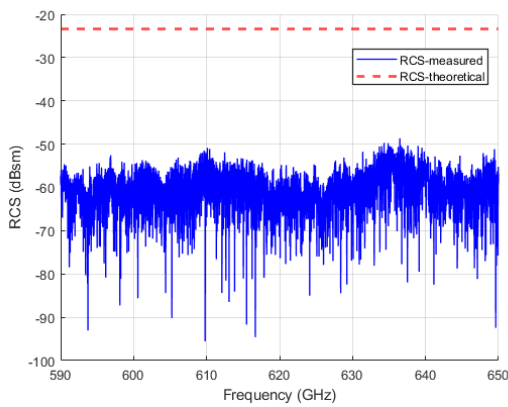


(a) No reference calibration

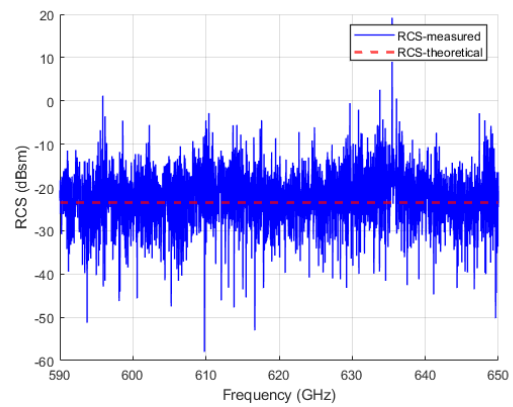


(b) Reference calibration

Figure 3.10: Range domain results of reference calibration via (3.5) vs. no calibration.



(a) No reference calibration



(b) Reference calibration

Figure 3.11: Frequency domain results of reference calibration via (3.5) vs. no calibration.

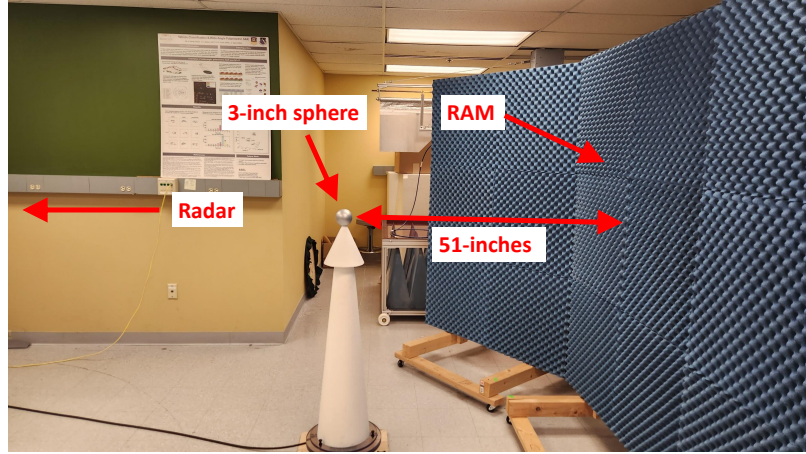


Figure 3.12: 3-inch sphere measurement setup.

3.3.3 Background Subtraction

Background subtraction is the process of subtracting a measurement of the target background from the target measurement as shown in (3.9) [34]. The goal of background subtraction is to remove the effects of scatterers besides the target of interest by simply taking an identical measurement without the target.

$$E_a^t(f) = E_m^t(f) - E_m^{tb}(f) \quad (3.9)$$

where $E_m^{tb}(f)$ is the response of the target background.

Combining (3.5) and (3.9) provides a target measurement that accounts for the frequency response of the measurement system and scattering from the background environment.

$$E_a^t(f) = \frac{E_m^t(f) - E_m^{tb}(f)}{E_m^r(f) - E_m^{rb}(f)} E_a^r(f) \quad (3.10)$$

Figures 3.13 and 3.14 show the effect of background subtraction with the reference calibration applied. It can be seen from Figure 3.13 that background subtraction via (3.10) reduces unwanted features from the measurement environment as well as lowers the general noise floor. Figure 3.14 shows that background subtraction in this case did not cause any

notable effect on the frequency domain data.

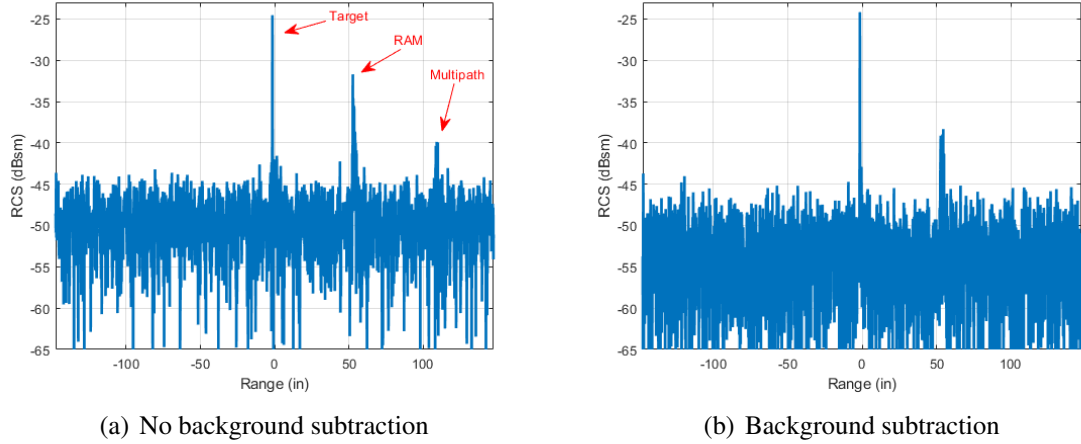


Figure 3.13: Range domain results of background subtraction via (3.10) vs. no background subtraction (3.5).

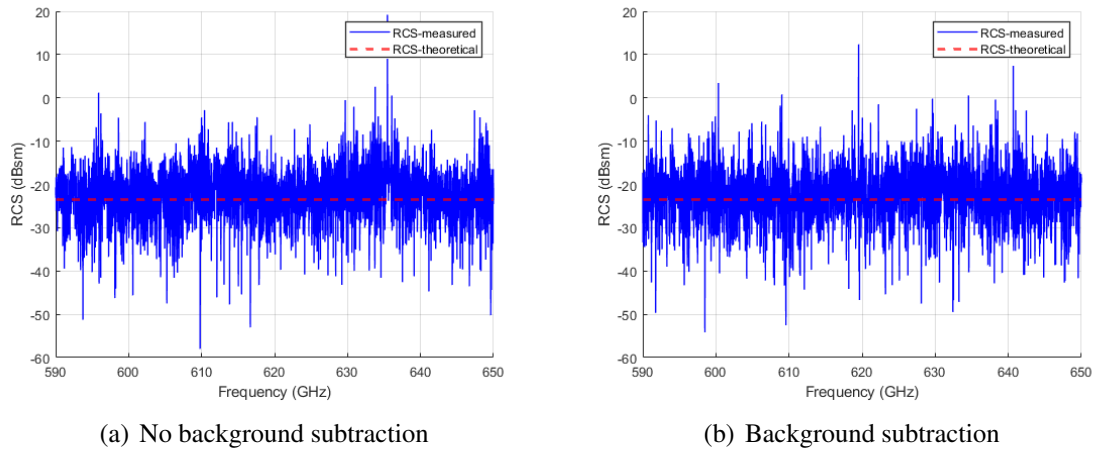


Figure 3.14: Frequency domain results of background subtraction via (3.10) vs. no background subtraction (3.5).

Using this scheme, five variables are needed to calculate the actual target response. The actual response of the reference target may be determined theoretically, by simulation, or from known specifications. The other four variables may be determined by measurement requiring four measurements. If the same test environment (including target mount) is used

for both the target and reference target then $E_m^{tb}(f) = E_m^{rb}(f)$ and only three measurements are required.

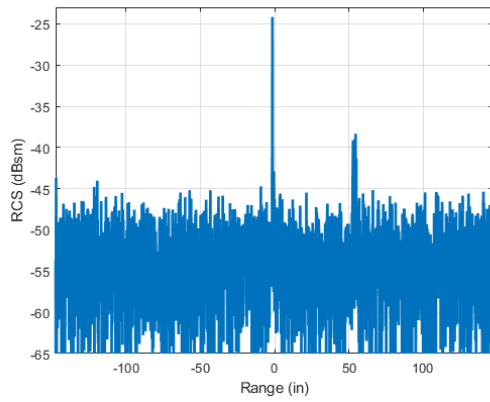
3.3.4 Range Gating

Another method used to improve RCS measurements is range gating. Range gating works by implementing a window function (called a “range gate”) in the range domain that preserves data from the range of interest while attenuating the response outside of that range. A range gate is set so that the response of the target is kept while the response of the background environment is suppressed. While implemented as a window function in range domain, range gating can also be implemented in the frequency domain as a convolution of the target response with the Fourier Transform of the window function. By setting the appropriate specifications, a filter can be designed in the frequency domain that provides the desired range gate.

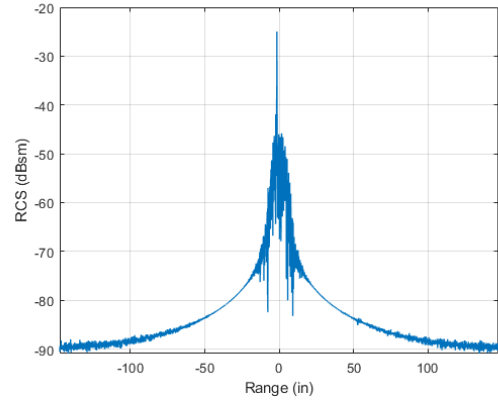
Combining range gating with reference target calibration and background subtraction provides the below equation for determining the RCS of a target, where $*$ is the convolution operator and $G(f)$ is the frequency domain of the range gate.

$$E_a^t(f) = \left(\frac{E_m^t(f) - E_m^{tb}(f)}{E_m^r(f) - E_m^{rb}(f)} E_a^r(f) \right) * G(f) \quad (3.11)$$

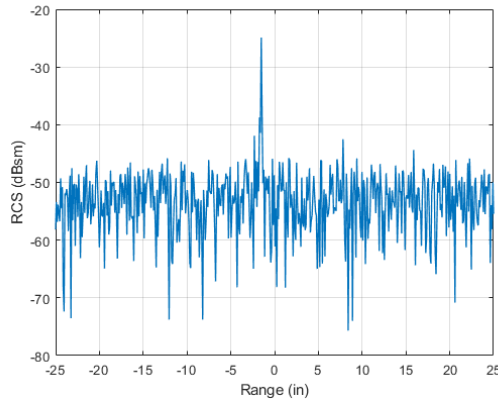
Figures 3.15 and 3.16 show the results of using a 6-inch range gate centered about the target via (3.11). It can be seen from the figures that using a range gate suppresses the response outside of the specified range and dramatically reduces the variance of the RCS measurement in the frequency domain. From figure 3.16 it is seen that implementation of the range gate significantly reduces the variance of the calculated RCS.



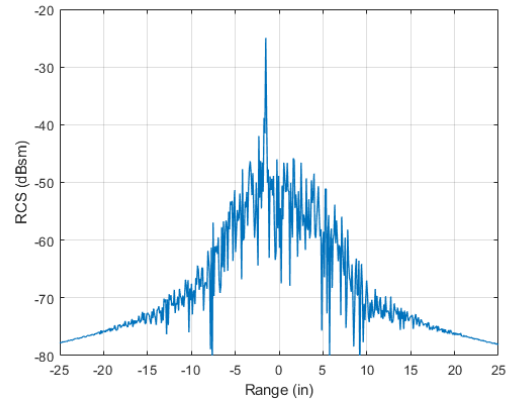
(a) No background subtraction



(b) Background subtraction

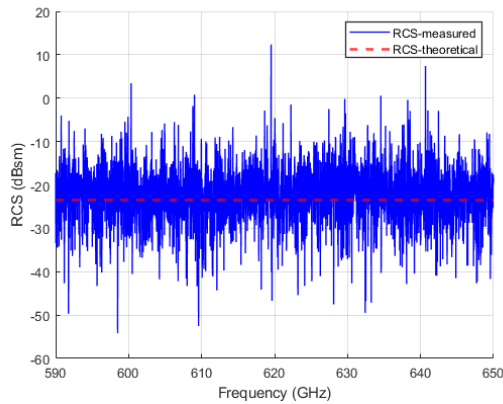


(c) No background subtraction

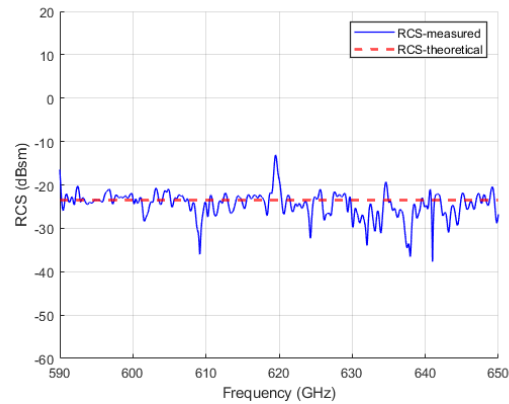


(d) Background subtraction

Figure 3.15: (a) and (c) show the results of using range gating (3.11) vs. not (3.10), respectively. (b) and (d) are close up views of (a) and (c), respectively.



(a) No range gate



(b) Range gate

Figure 3.16: Frequency domain results of range gating (3.11) vs. not (3.10).

3.4 Scale Model Surface Roughness Experiment

3.4.1 Experiment Overview

An experiment is designed to investigate the effects of varying surface roughness on scale model measurements. Four aluminium dihedrals are machined, one dihedral is designed for Ka-band measurements and three THz scale models are made with varying roughness. One sample is as machined using standard end mill cutting, one is hand-polished using a Scotch Bright pad, and one is bead blasted using heavy grit via air pressure. These three different finishing techniques provide varying surface roughness on otherwise identical models. The THz scale models will be measured and used to predict the RCS of the full-size Ka-band target. The rest of this section describes the targets, the experiment parameters and how the results will be determined.

3.4.2 Dihedral Targets

The four aluminium dihedrals were manufactured by Triangle Precision Industries, Inc. located in Dayton, Ohio. Table 3.3 lists the inside face dimensions as well as what surface treatment, if any, was done to the sample. Each dihedral is 1/8 inch thick. Figure 3.17 shows the dihedral geometry.

Table 3.3: Dihedral Manufacturing Specifications

Name	L (in)	H (in)	Treatment
THz polished	0.5	0.25	Scotch Bright Pad hand polish
THz normal	0.5	0.25	No finish
THz rough	0.5	0.25	Heavy grit bead blast via air pressure
Ka normal	9.0909	5.5	No finish

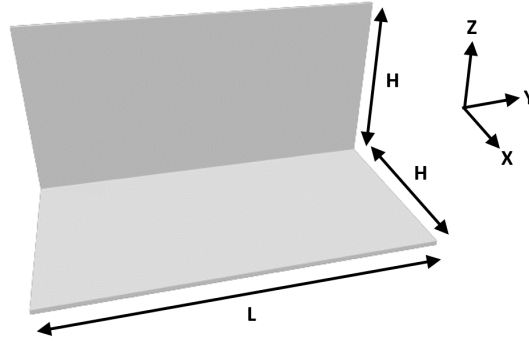


Figure 3.17: Dihedral geometry.

The surface roughness of each dihedral was measured using a Mitutoyo SJ-210 surface roughness tester. Table 3.4 lists the surface roughness data measured for each dihedral. The roughness parameters are defined as follows, where Z_i represents the deviation of each surface height sample from the mean surface height: R_a is the arithmetical mean of the absolute values of the profile deviations (Z_i) from the mean line of the roughness profile. R_z is an algorithm that splits the collection length into five sections and computes the average of the maximum peak to valley distance of each section [36]. Note that the wavelength at 600 GHz is on the order of 19,000 μin , much larger than the roughness parameters of the test targets.

Table 3.4: Dihedral surface roughness

Name	R_a (μin)	R_z (μin)
THz polished	17.14	114.21
THz normal	19.41	121.10
THz rough	218.08	1257.75
Ka normal	15.16	97.13

3.4.3 Experiment Parameters

Table 3.5 lists the measurement parameters for the THz scale model targets. Each target will be aligned so that the peak specular response occurs at 0 degrees azimuth. The targets are mounted at a 45-degree forward pitch and measured at a range of 1.6 meters. This range provides a beamwidth of 8 inches at the target area which allows for the full illumination of a three-inch sphere which is used as the calibration target. Due to the high frequency of the measurement the geometry of the setup does not meet the general far field range requirement of the sphere (which is 25 meters using the common approximation $\frac{2D^2}{\lambda}$, where D is the maximum target dimension).

Table 3.5: Scale Model Measurement Specifications

Frequency range	590-650 GHz
Frequency step size	30 MHz
PNA IF bandwidth	10 kHz
Azimuth range	-3.5 - 3.5 deg
Azimuth step size	0.1 deg
Averaging	None
Tx elevation angle	-0.7 deg
Rx elevation angle	1 deg
Range	1.6 m

Figure 3.18 shows one of the dihedrals mounted on the pedestal. A styrofoam block is used to support the dihedral which is carefully set in position with the correct 45-degree pitch. A laser boresight aligner is used to align the transmit and receive antennas to the center of the dihedral.



Figure 3.18: Scale model dihedral mounted on foam pedestal.

The Ka-band dihedral is measured using the same dihedral orientation and transmit and receive angles as the THz models. The same N5224A network analyzer is used with two Ka-band antennas to make the measurements, which are processed using the same techniques as described in Section 3.3. Table 3.6 lists the Ka-band measurement parameters. At a range of 2.5 meters the dihedral is fully illuminated by the measurement system, but is not far enough to be in the dihedral’s far field (14 meters). The range is limited by the size of the measurement lab.

Table 3.6: Ka-band Measurement Specifications

Frequency range	26.5-40 GHz
Frequency step size	30 MHz
PNA IF bandwidth	10 kHz
Azimuth range	-3.5 - 3.5 deg
Azimuth step size	0.1 deg
Averaging	None
Tx elevation angle	-0.7 deg
Rx elevation angle	1 deg
Range	2.5 m

Figure 3.19 shows the dihedral mounted on the pedestal. The dihedral is mounted using the same process as for the scale models.



Figure 3.19: Ka-band dihedral mounted on foam pedestal.

3.4.4 Parametric Scattering Model

The parametric scattering model presented by Jackson et al. [37] is chosen for evaluating the accuracy of the RCS measurements of the three scale model targets as well as that of the full size target. This model has been validated for predicting the mainlobe response of the dihedral by comparison to measured data at the Air Force Institute of Technology (AFIT) indoor range as well as various numerical simulation techniques including method of moments (MoM), finite integration technique (FIT) and shooting and bouncing rays (SBR) [38]. The parametric scattering model is straightforward to implement and can be calculated for any dihedral orientation and bistatic measurement geometry.

Using this model, the amplitude response of the dihedral is calculated as

$$|M_{dih}(\Theta_{dih})| = \left| \frac{jk2LH}{\sqrt{\pi}} \right| \text{sinc} \left[\frac{kL}{2} (\sin \phi_t \cos \theta_t + \sin \phi_r \cos \theta_r) \right] \\ \times \text{sinc} [kH (\cos \theta_t - \cos \theta_r)] \begin{cases} \sin \left(\frac{\theta_t + \theta_r}{2} \right), \theta_t, \theta_r \in \left[0, \frac{\pi}{4} \right] \\ \cos \left(\frac{\theta_t + \theta_r}{2} \right), \theta_t, \theta_r \in \left[\frac{\pi}{4}, \frac{\pi}{2} \right] \end{cases}, \quad (3.12)$$

where L and H are the dihedral dimensions and $\Theta_{dih} = \{L, H, \theta_t, \phi_t, \theta_r, \phi_r\}$ represents all of the dependant variables [38]. For a rotated dihedral, a coordinate transformation can be applied to produce results for whatever transmitter/receiver/dihedral geometry is desired. Jackson et al. describe this process and the effects of polarization in greater detail in [37]. Because this model is specifically validated for the mainlobe response, only the mainlobe response of the dihedrals will be compared to the model for evaluation.

3.5 Analysis Method

The measured RCS of the THz and Ka-band dihedrals will be compared to the parametric scattering model. The peak specular response error for each target will be defined as

$$\epsilon_{peak} = |\sigma_{PM} - \sigma_{meas}| \quad (3.13)$$

and the relative error defined as

$$\epsilon_{peak} = \frac{|\sigma_{PM} - \sigma_{meas}|}{\sigma_{PM}}, \quad (3.14)$$

where σ_{PM} is the computed RCS using the parametric scattering model and σ_{meas} is the measured RCS. This error term will be provided in units of m^2 . To compare the specular

scattering as a function of azimuth angle the error will also be plotted as a function of azimuth.

Second, the scale models will be used to predict the RCS of the Ka-band dihedral via (2.3) using a scale factor of $s = 33/600$. The predicted RCS will be compared to both the parametric scattering model and the measured RCS using the same error definitions given by (3.13) and (3.14). An error vs. azimuth plot will also be provided.

Results

4.1 Introduction

This chapter provides the results of the experiment described in Chapter 3. Section 4.2 presents the measured RCS of a three-inch diameter conducting sphere and the results of an ISAR experiment demonstrating the ability of the system to conduct ISAR measurements. Section 4.3 presents the results of the THz dihedral measurements.

4.1.1 A Note on Accuracy

The measured values presented and used for error calculations in this paper are taken directly from the prototype measurement system as is. A study on the system's accuracy has yet to be completed. This paper uses comparison between measurement data and the parametric scattering model as a sanity check but does not make any claims of achieving a certain repeatable accuracy. The number of digits used when reporting results does not intend to imply a certain level of accuracy or precision. A thorough study on the accuracy and precision of the system is warranted.

4.2 THz Measurement System Performance

4.2.1 3-Inch Sphere RCS

The RCS of a 3-inch diameter sphere is measured using a 6-inch diameter sphere as the reference target. The 3-inch sphere has a theoretical RCS of -23.41 dBsm for a perfect conductor. Figure 4.1 shows the range profile for the sphere with a 6-inch wide range-gate centered at the center of the sphere. A peak RCS of -24.9632 dBsm is computed from the measured data range profile. This measurement has a calculated error of 13.7 cm².

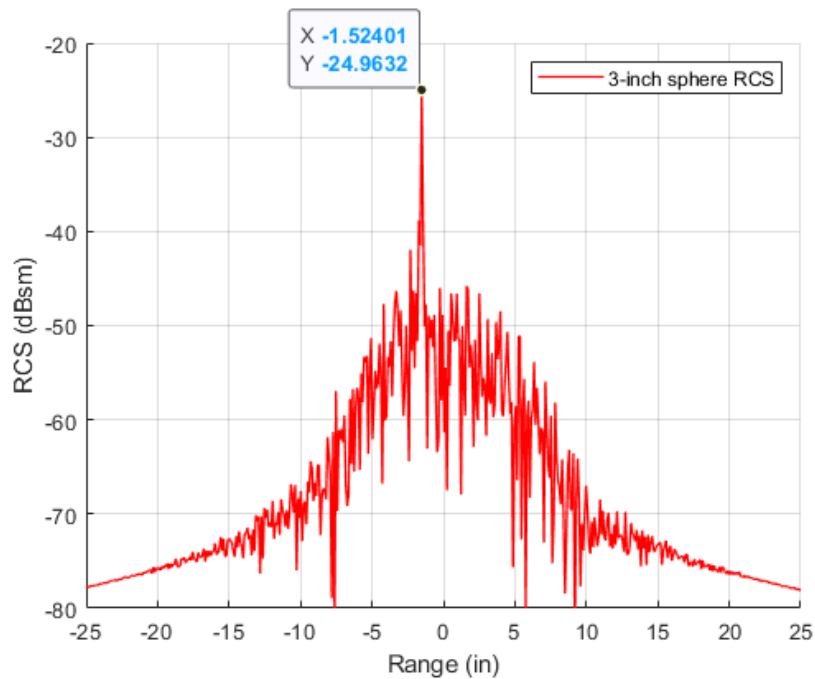


Figure 4.1: Range profile for 3-inch sphere.

Figure 4.2 shows the calculated RCS of the sphere as a function of frequency. The mean RCS over the measured frequency range is -24.52 dBsm. The mean error across the frequency domain for this measurement is 10.28 cm². As stated previously, the accuracy of the measurement system itself is still unknown at this point.

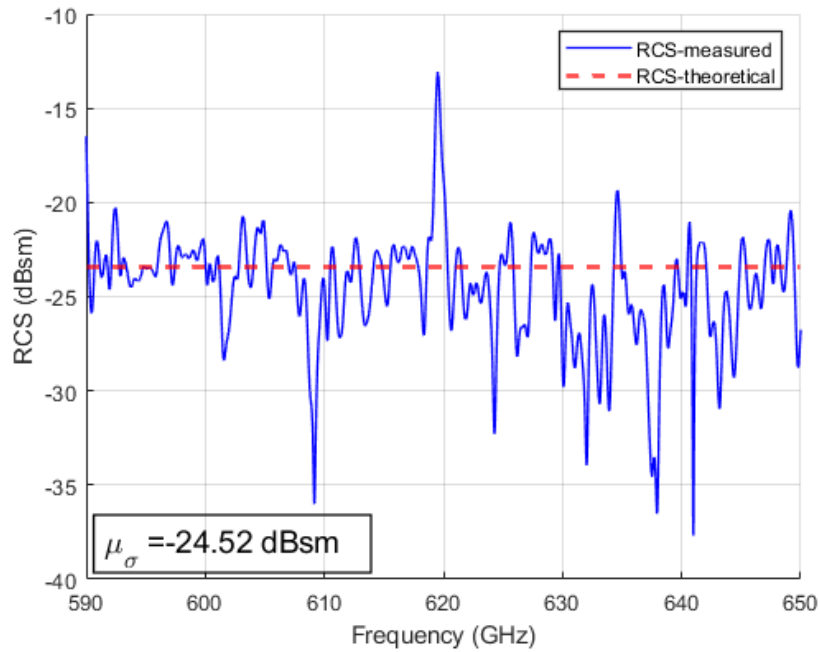


Figure 4.2: Measured RCS of 3-inch sphere.

4.2.2 ISAR Imaging

To demonstrate the ISAR capabilities of the system an experiment was designed with the parameters listed in Table 4.1.

Table 4.1: ISAR Experiment Parameters

Frequency range	590-650 GHz
Frequency step size	20 MHz
Angular span	5.8 degrees
Angular step size	0.02 degrees
IF bandwidth	30 kHz
Depression angle	25.5 degrees
Range to target	100.5 inches
Bistatic angle	0.855 degrees
Experiment run time	1132 seconds

Figure 4.3 shows the distribution of corner reflector targets arranged in the shape of the letter “A” on the pallet.

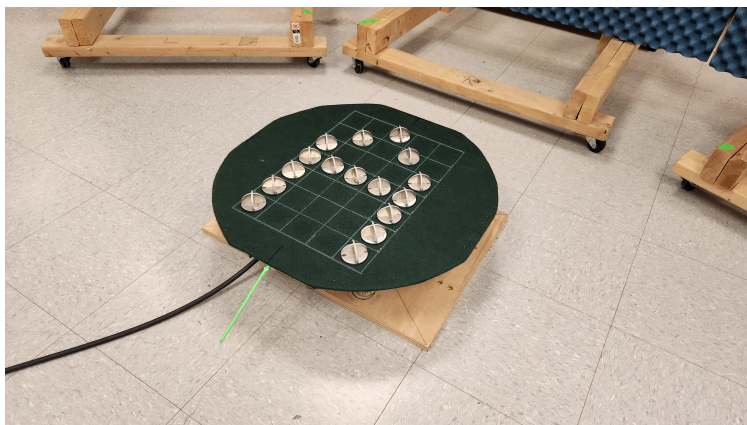


Figure 4.3: ISAR measurement for letter “A”.

Figure 4.4 shows the physical experiment setup with annotated geometry.

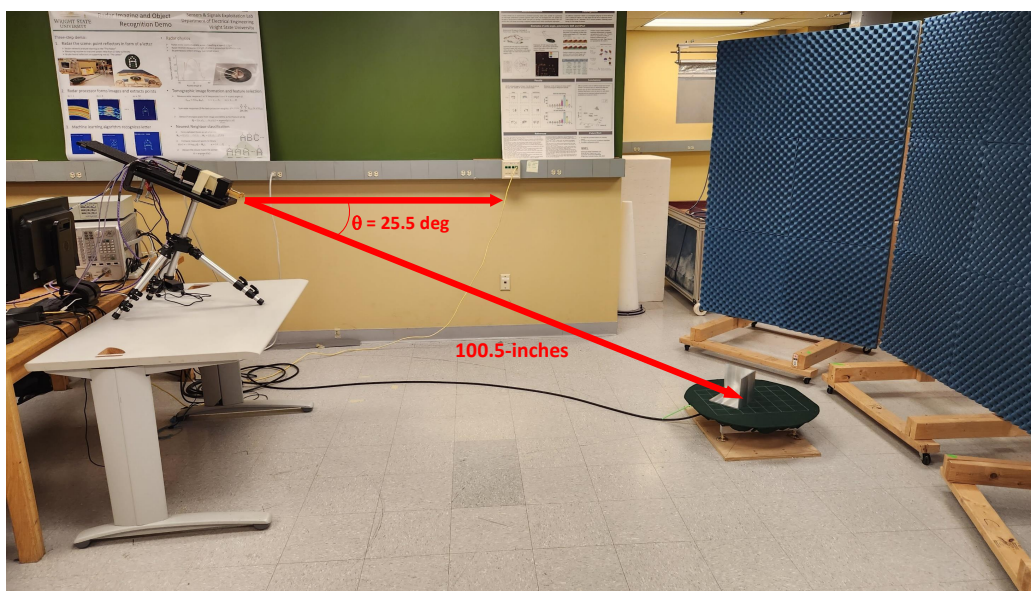


Figure 4.4: Experiment geometry for “A” measurement.

Figure 4.5 shows the ISAR image computed using the polar format algorithm (PFA). The top 30-dB of the normalized ISAR results are shown and the letter “A” is clearly identifiable.

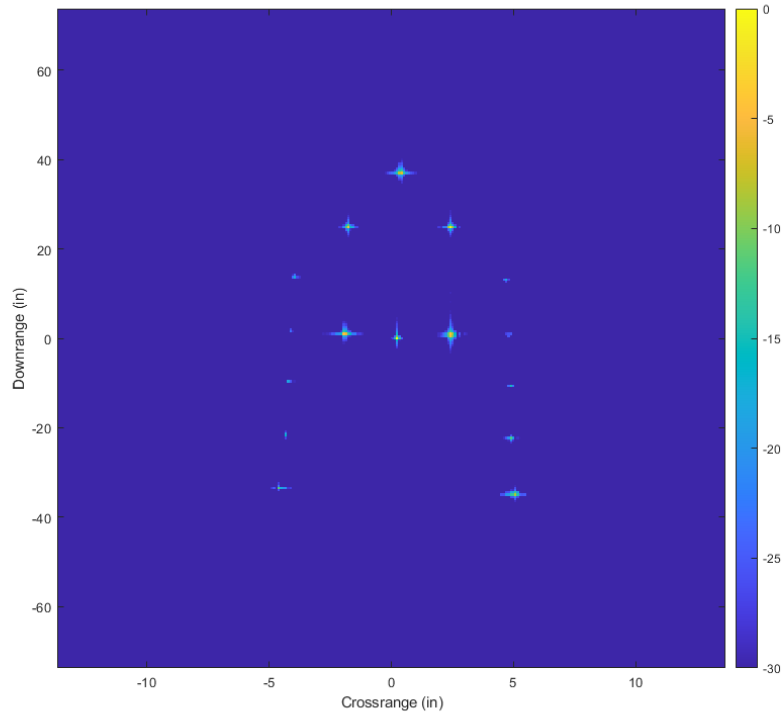


Figure 4.5: “A” ISAR image.

4.3 THz Dihedral Measurement Results

Figures 4.6-4.14 show the results of the scale model RCS measurements via (3.11), the parametric model results via (3.12), and the error via (3.13). Recall that the parametric model has only been validated for the mainlobe response. The sidelobes are shown to provide a comparison of the model to the measured response, but are not considered in the error analysis. These plots are shown for each scale model at 600, 625 and 650 GHz to demonstrate results over the bandwidth used. It is seen that for all models the error at 625 GHz is larger (by at least 0.03 m^2) than at 600 or 650 GHz.

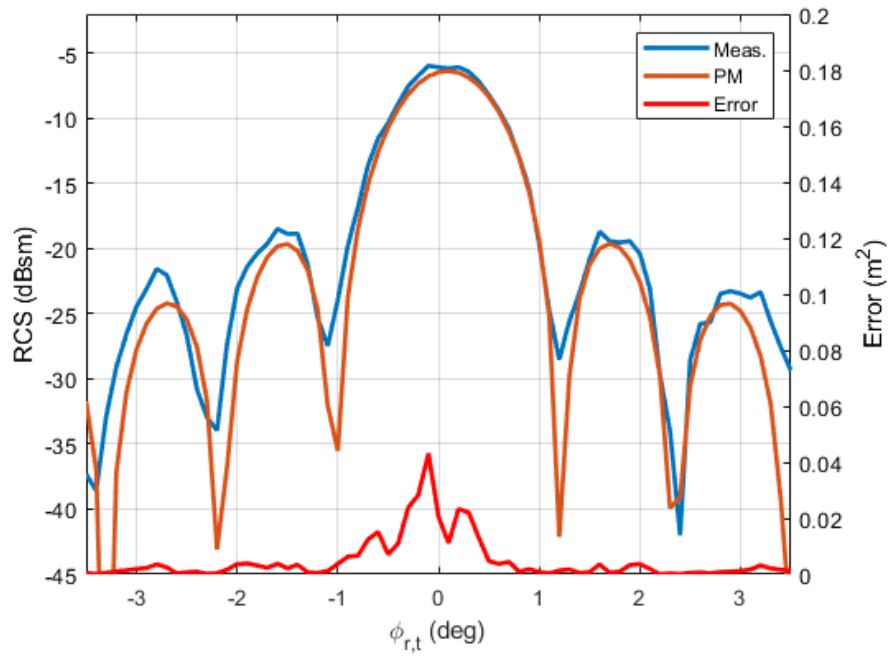


Figure 4.6: Polished scale model dihedral results at 600 GHz.

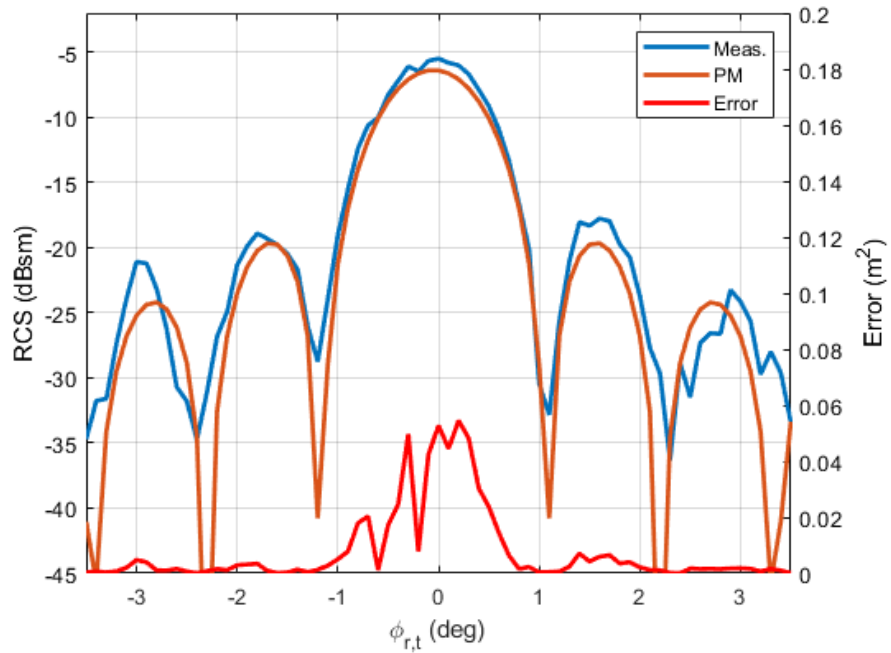


Figure 4.7: Normal scale model dihedral results at 600 GHz.

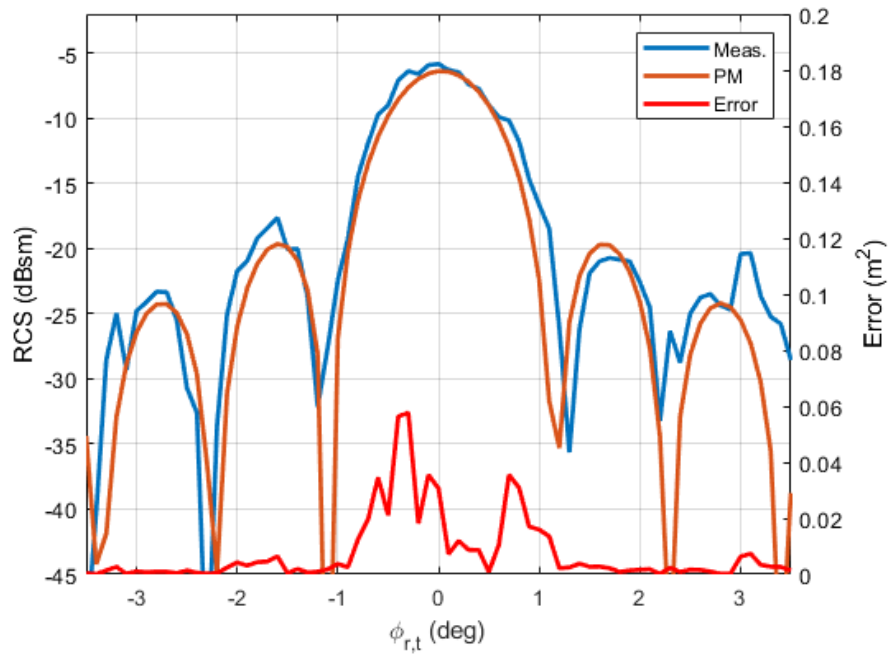


Figure 4.8: Rough scale model dihedral results at 600 GHz.

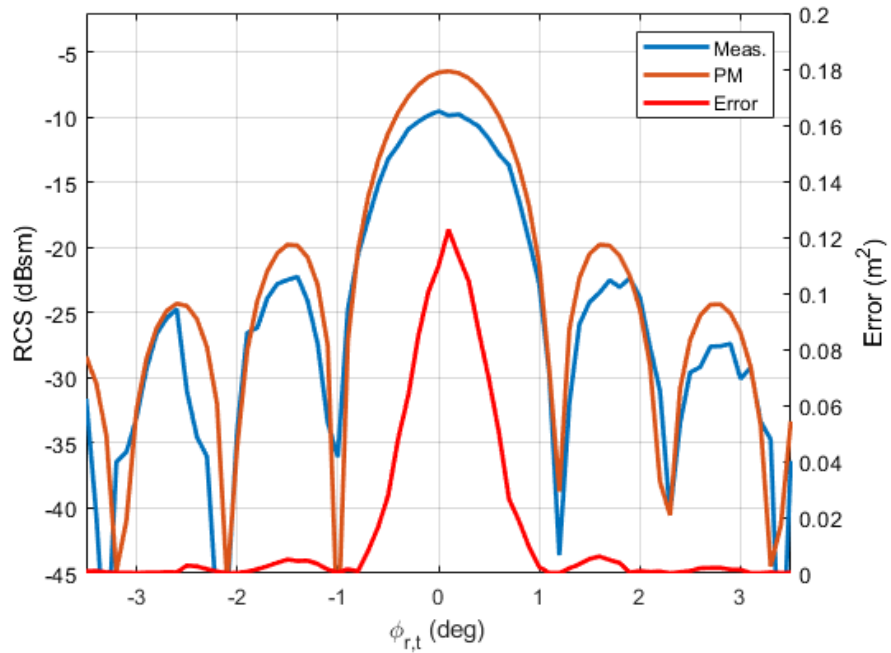


Figure 4.9: Polished scale model dihedral results at 625 GHz.

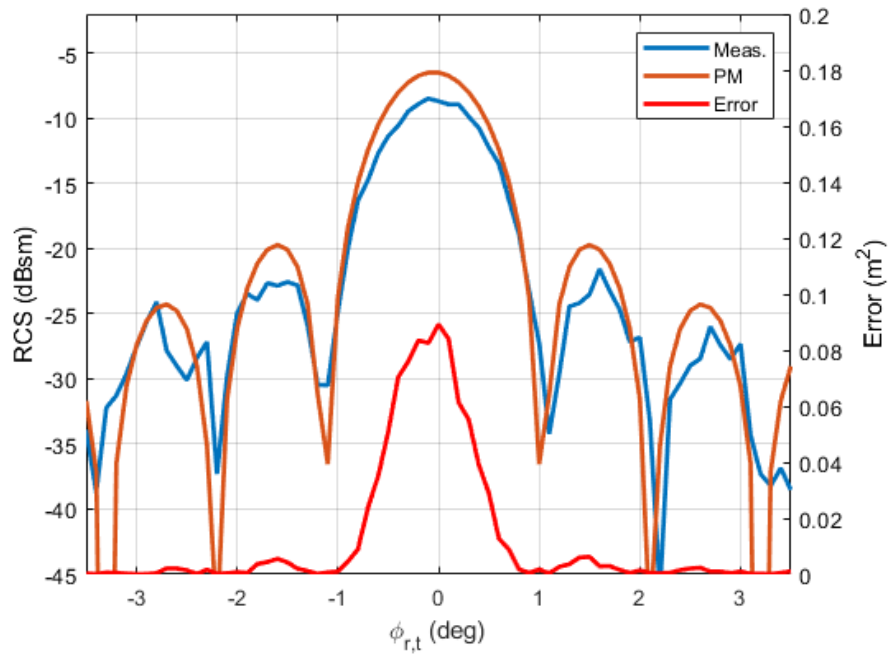


Figure 4.10: Normal scale model dihedral results at 625 GHz.

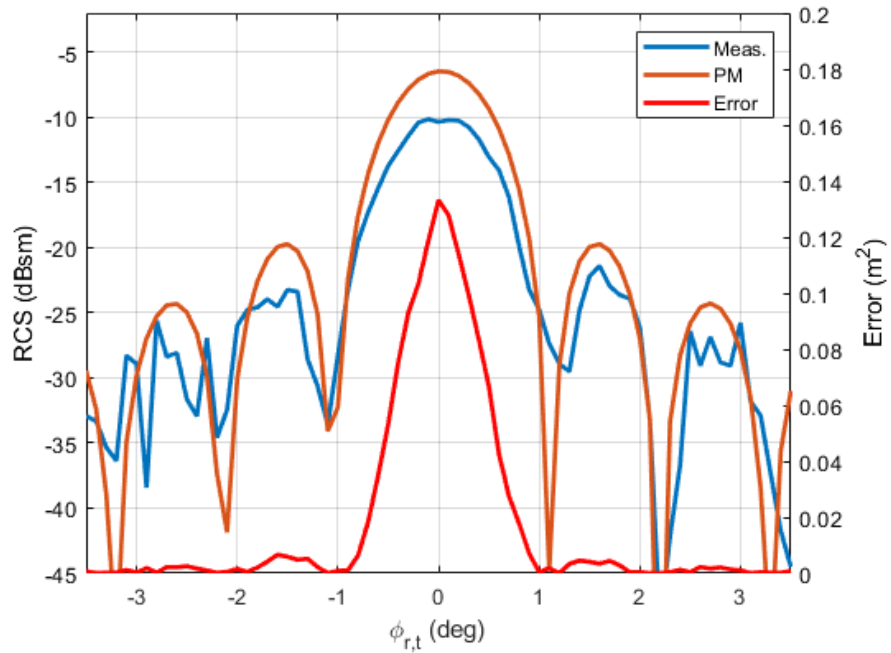


Figure 4.11: Rough scale model dihedral results at 625 GHz.

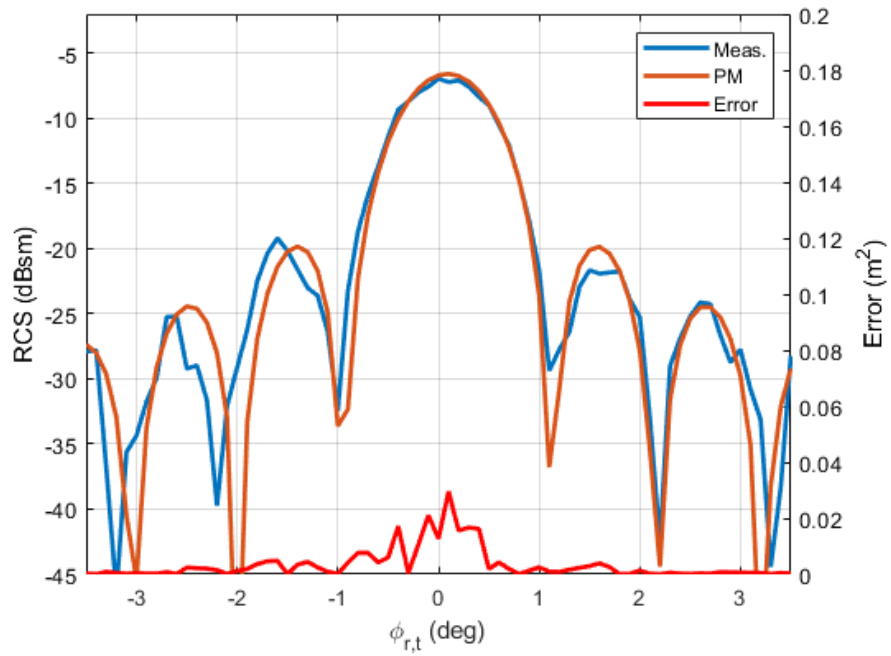


Figure 4.12: Polished scale model dihedral results at 650 GHz.

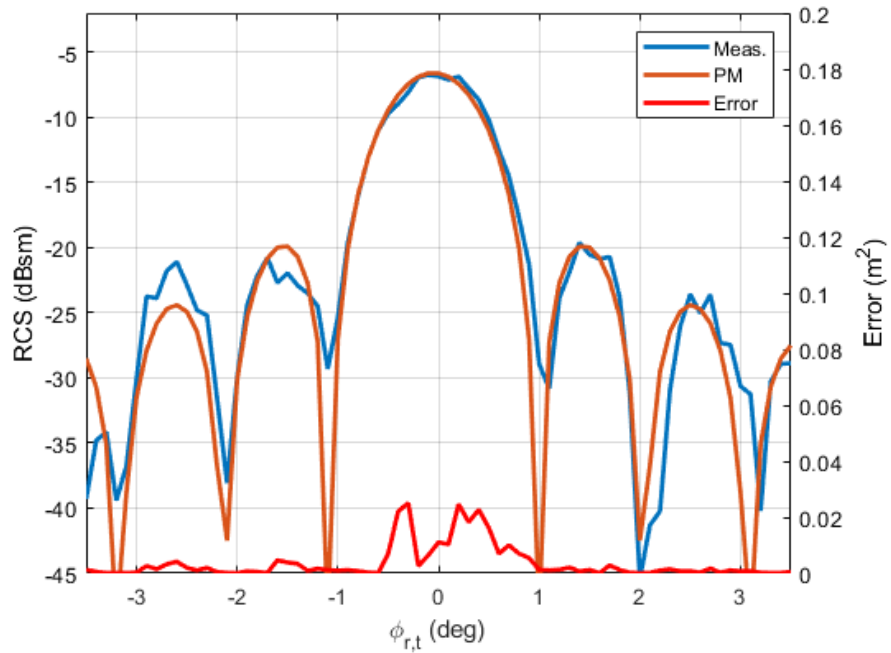


Figure 4.13: Normal scale model dihedral results at 650 GHz.

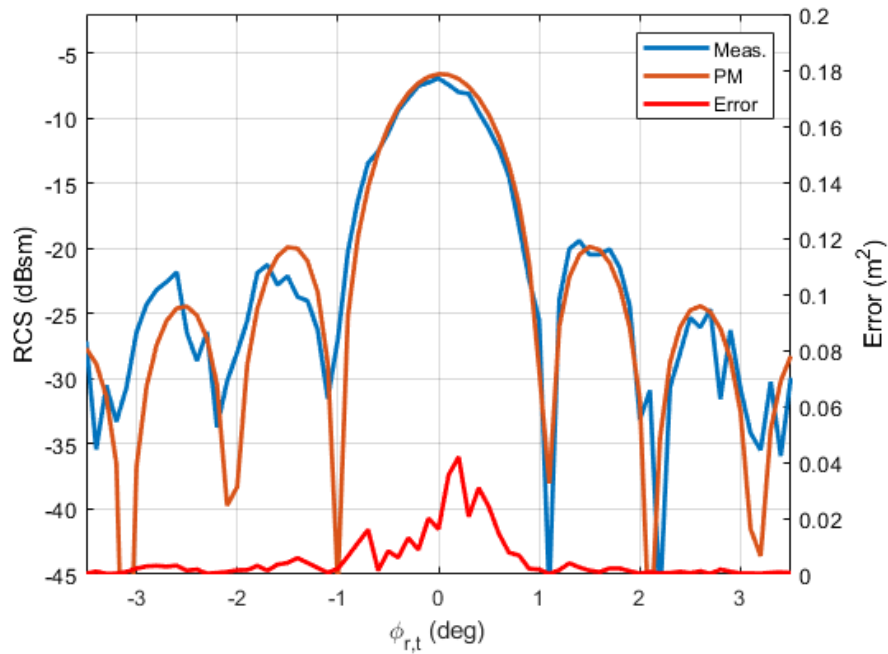


Figure 4.14: Rough scale model dihedral results at 650 GHz.

Figures 4.15-4.20 show the error via (3.13) and relative error via (3.14) for each model's peak response as a function of frequency. The mean error or mean relative error is plotted as a red dashed line in each figure. It is seen from the figures that the measurement error varies noticeably with frequency. The similarities between the error (one dominant peak at 613 GHz, similar pattern for the rest of the data) for each model suggest that this error is not simply random noise but may have a common unknown cause.

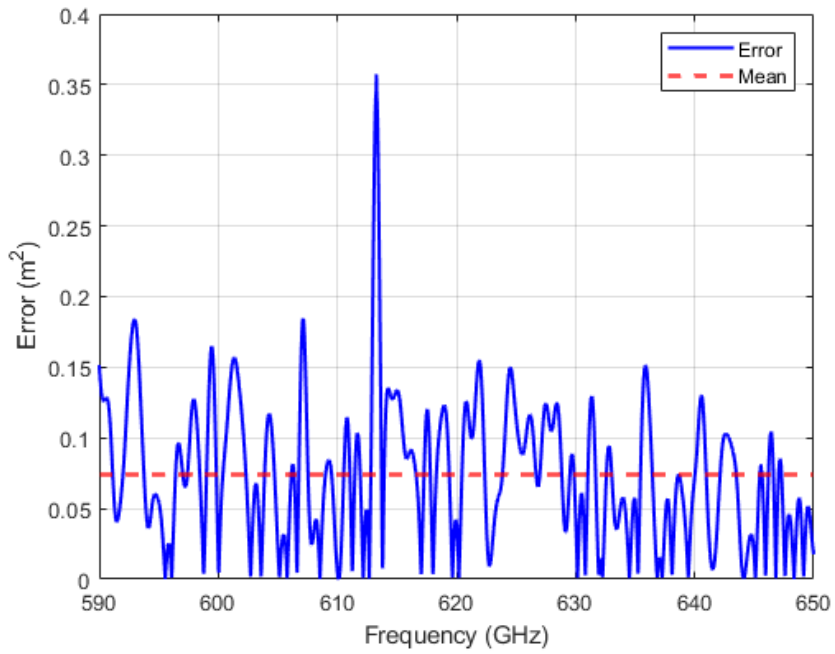


Figure 4.15: Polished scale model error.

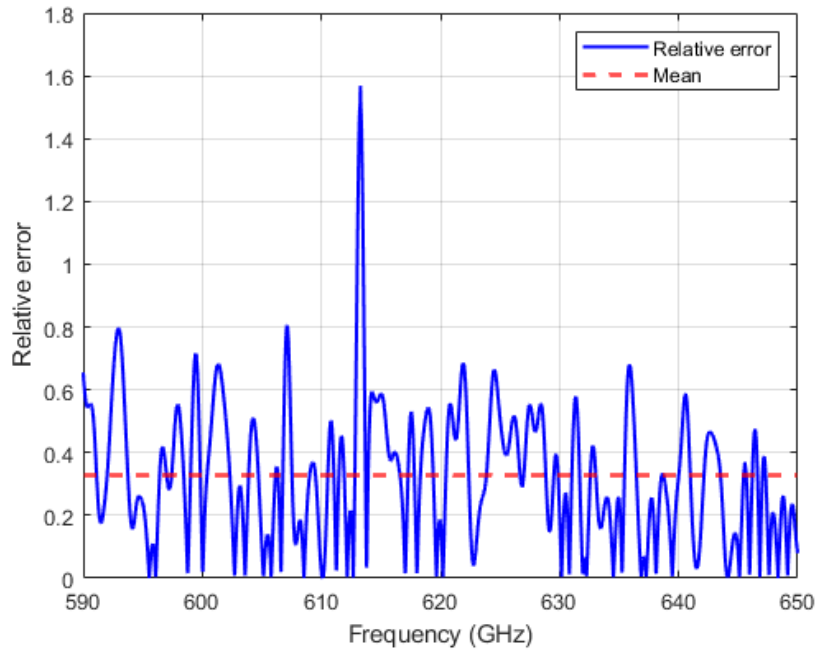


Figure 4.16: Polished scale model relative error.

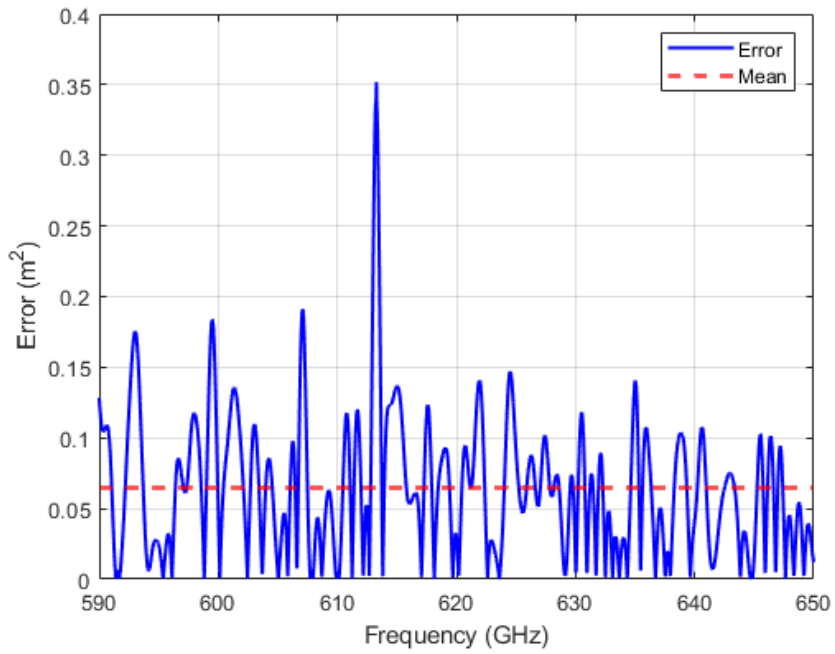


Figure 4.17: Machined scale model error.

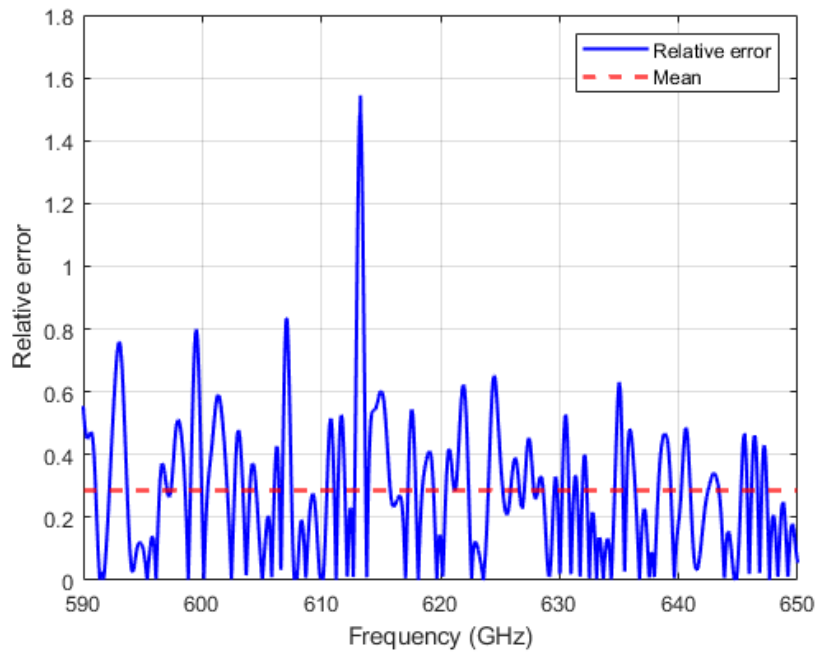


Figure 4.18: Machined scale model relative error.

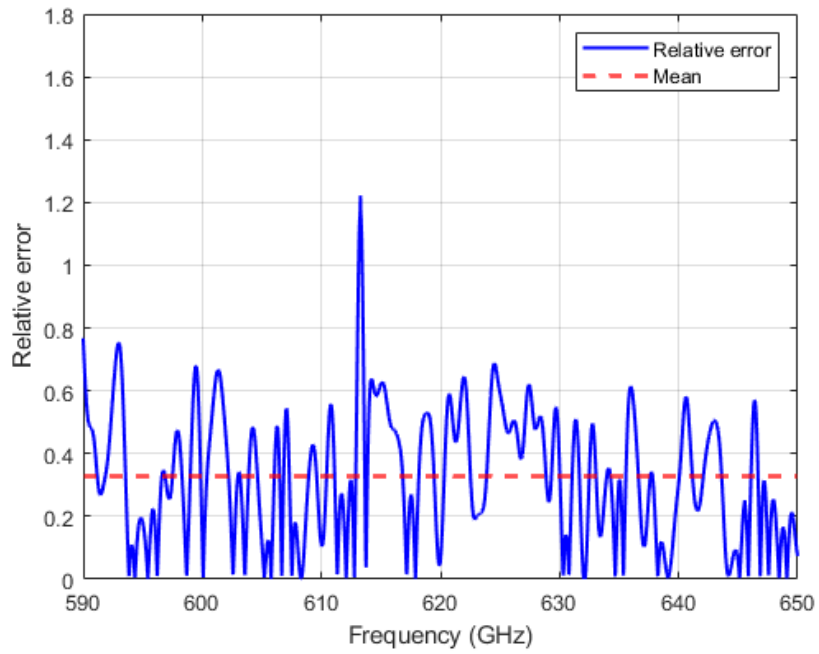


Figure 4.19: Rough scale model error.

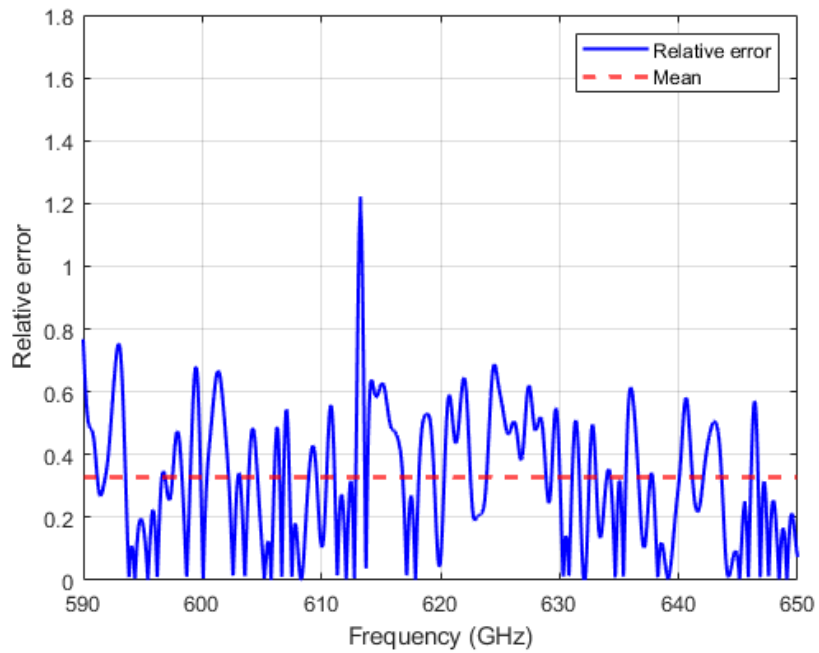


Figure 4.20: Rough scale model relative error.

Table 4.2 lists the mean error and mean relative error over the entire frequency range

measured for each scale model. The maximum error is 0.074 m² and the maximum relative error is 0.328. The machined model has the smallest mean relative error across the frequency range, followed by the polished model and then the rough model. The mean relative error varies from 0.284 to 0.328.

Table 4.2: Scale Model Error

Sample	Error (m ²)	Relative Error
Polished	0.074	0.327
Machined	0.064	0.284
Rough	0.074	0.328

4.4 Ka-band Dihedral Measurement Results

Similar to figures 4.6-4.14, Figures 4.21-4.23 show the error via (3.13) and relative error via (3.14) for the Ka-band target at 33, 34.375 and 35.752 GHz, which are the scaled frequencies given in the aforementioned figures ($f_{Ka} = s f_{THz}$). It is seen that the measured results are noticeably different than the model results. This behavior is similar to that noted by Knott in section 4.2 of [21] when the target is not sufficiently far from the measurement system. Knott demonstrates that when the system is not sufficiently in the far field of the test target the peak response is reduced in amplitude, the sidelobes rise an amplitude, and the nulls fill. The Ka-band target was not placed beyond the it's far field due to space limitations, which is a likely explanation for this behavior. New data should be measured with the target at a farther range to observe if this behavior is reduced.

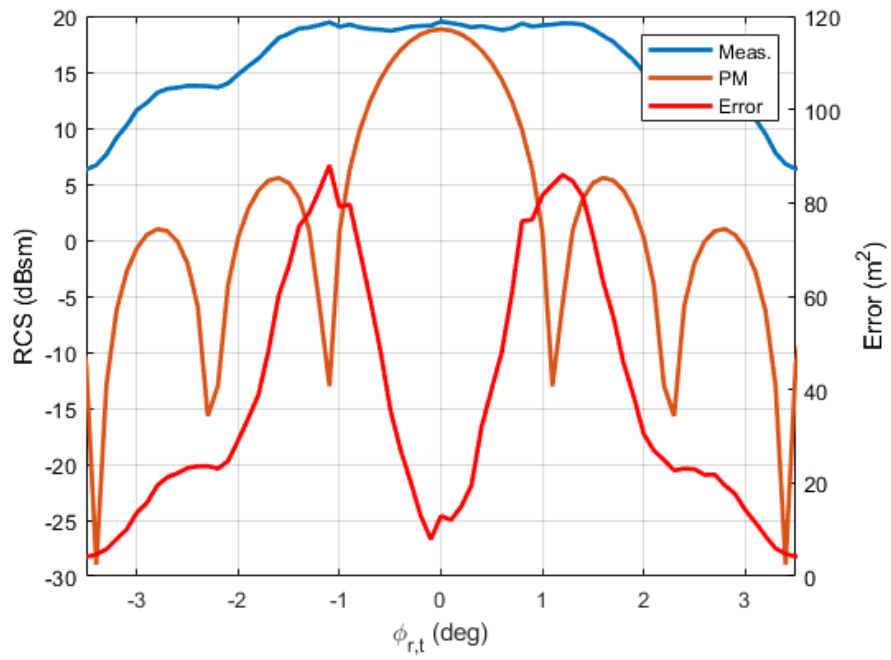


Figure 4.21: Ka-band dihedral results at 33 GHz.

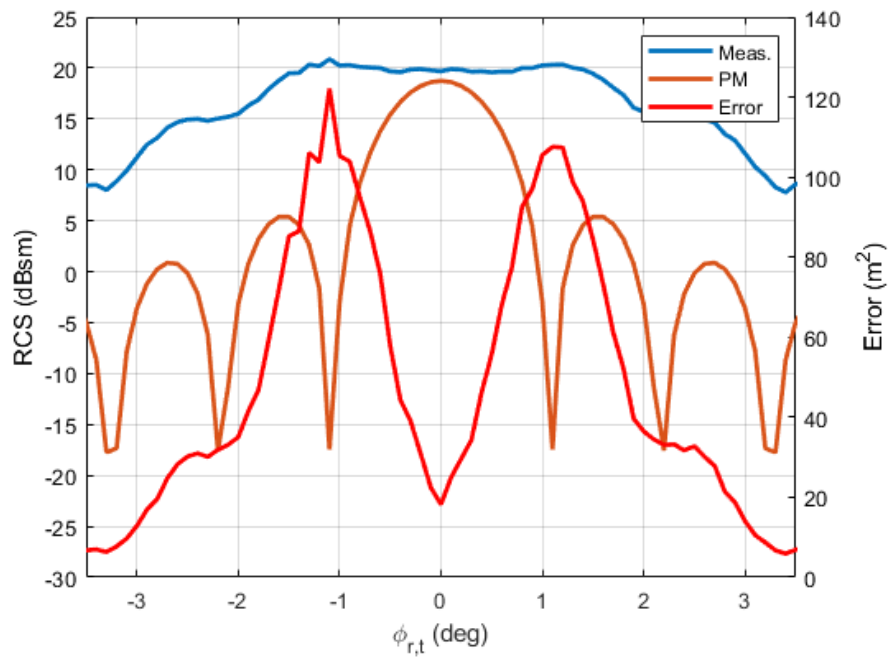


Figure 4.22: Ka-band dihedral results at 34.375 GHz.

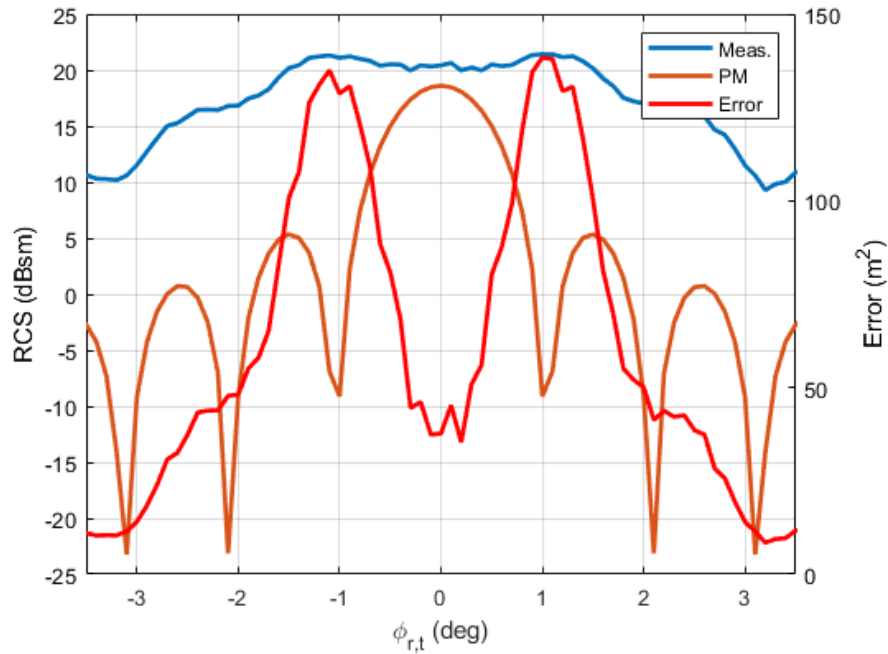


Figure 4.23: Ka-band dihedral results at 35.752 GHz.

4.5 Comparison of Scale Model Prediction to PM

Similarly to Figures 4.6-4.14, Figures 4.24-4.32 show the results of the Ka-band RCS prediction via scale model measurements compared to the parametric model results. These plots are shown for each scale model at 33, 34.375 and 35.752 GHz. It is seen that for all models the error at 34.375 GHz is larger (by at least 10 m²) than at 33 or GHz. This is similar to the 625 GHz measurements at having the largest error, which is to be expected since that same data was used to calculate these prediction. The scale model error translates to error in the prediction.

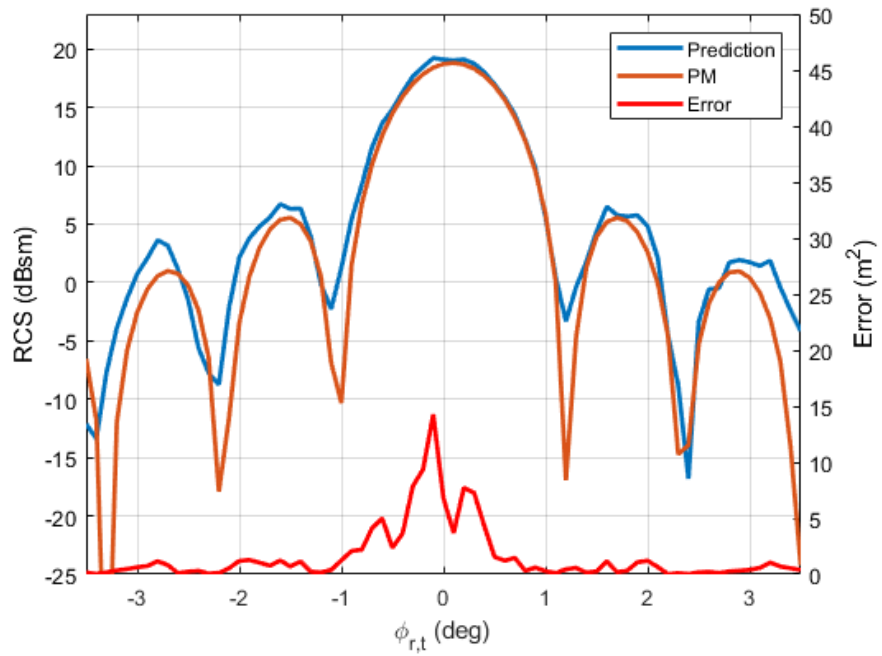


Figure 4.24: Polished scale model prediction results at 33 GHz.

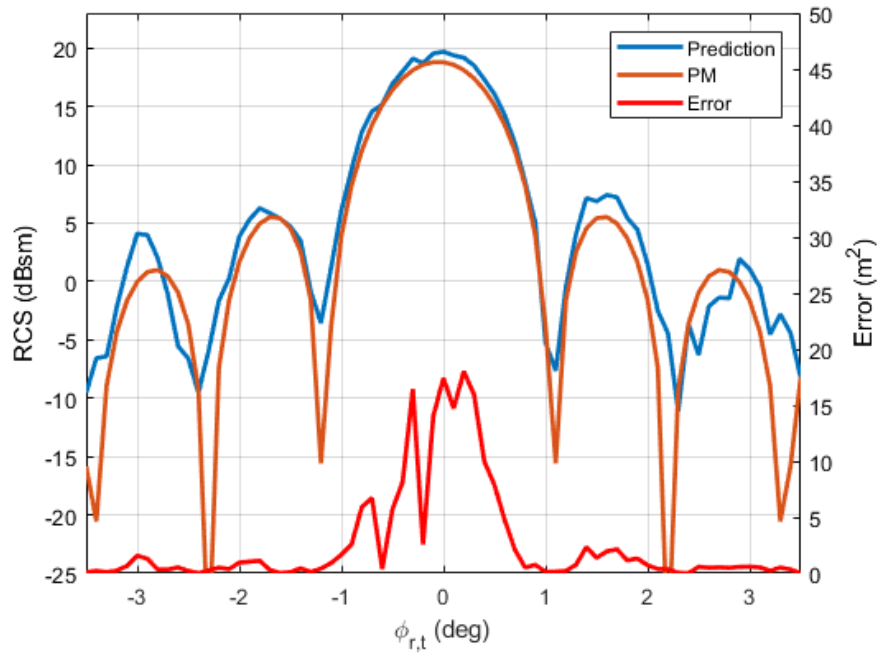


Figure 4.25: Normal scale model prediction results at 33 GHz.

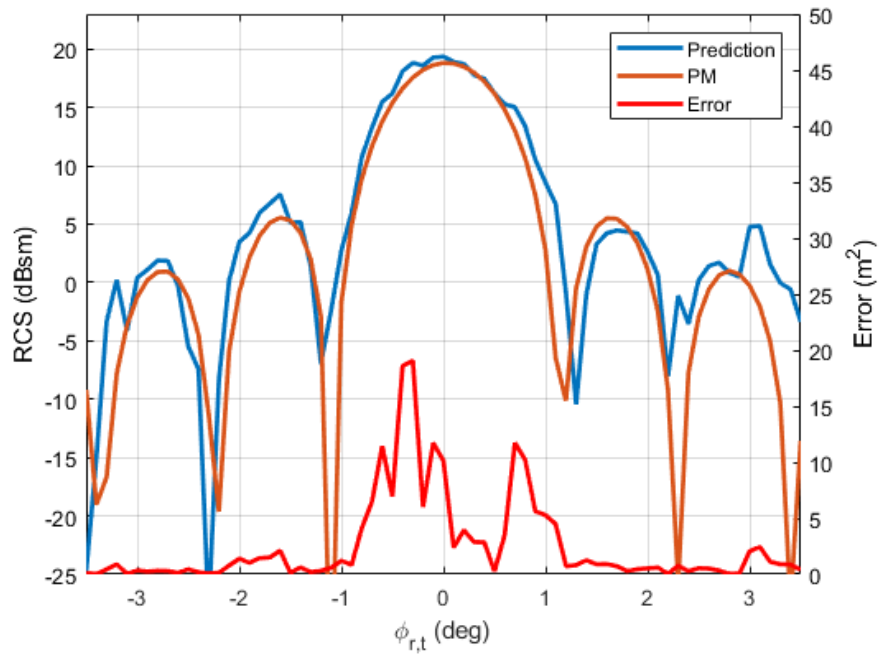


Figure 4.26: Rough scale model prediction results at 33 GHz.

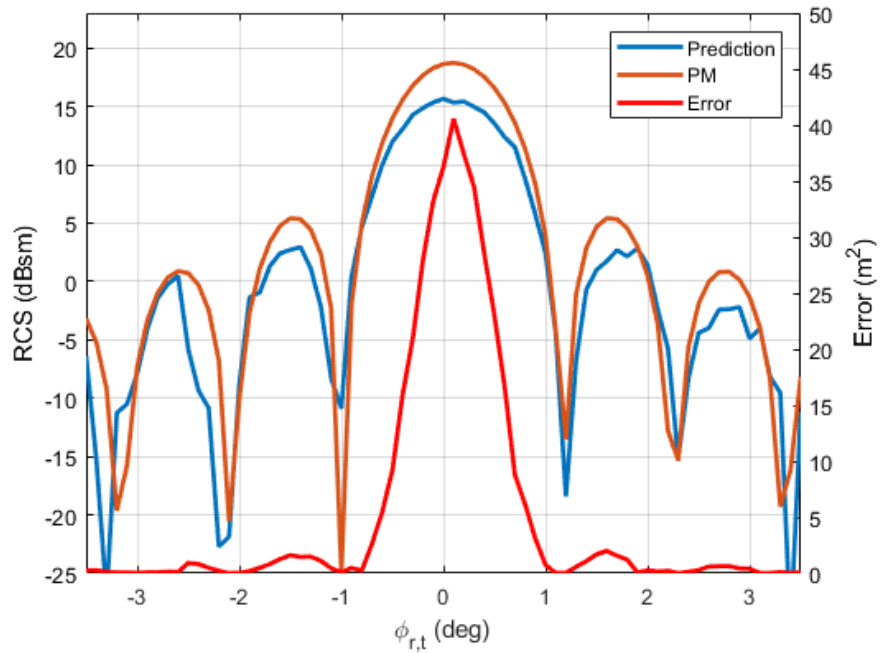


Figure 4.27: Polished scale model prediction results at 34.375 GHz.

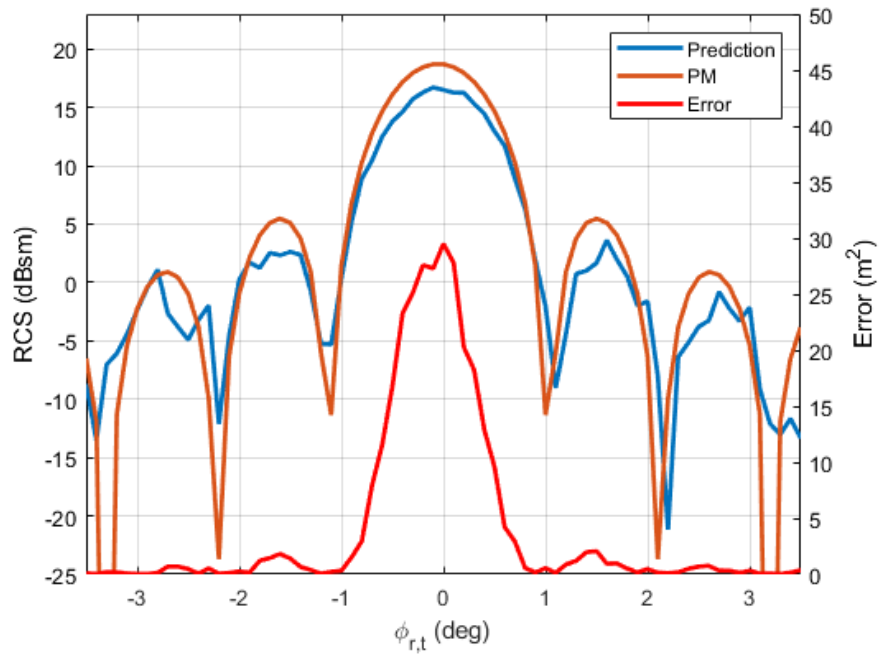


Figure 4.28: Normal scale model prediction results at 34.375 GHz.

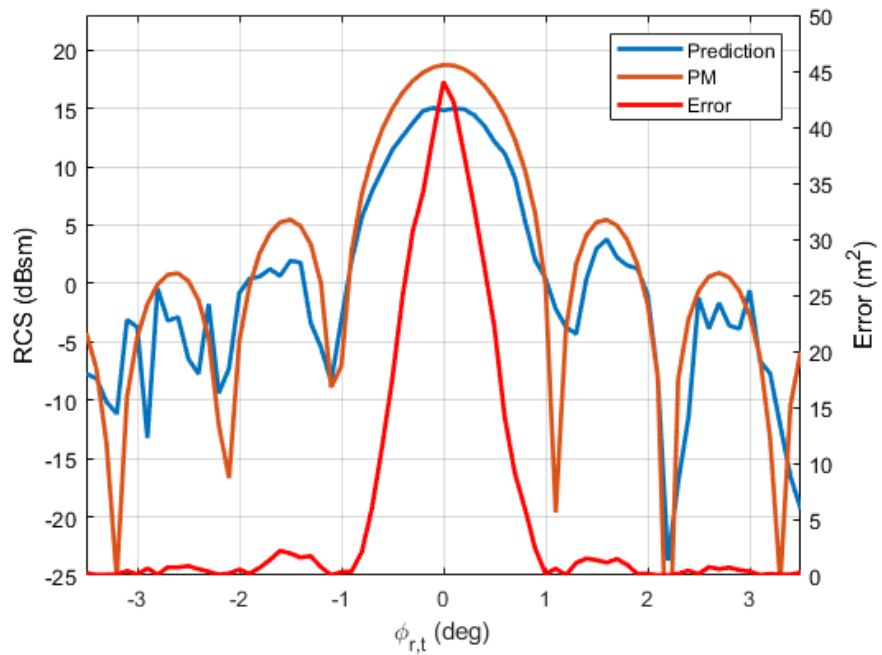


Figure 4.29: Rough scale model prediction results at 34.375 GHz.

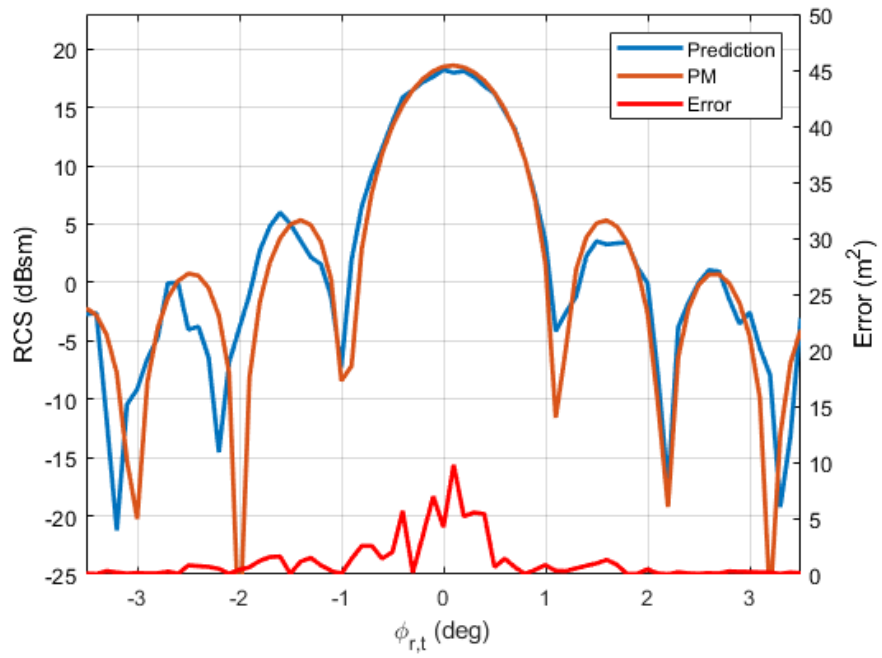


Figure 4.30: Polished scale model prediction results at 35.752 GHz.

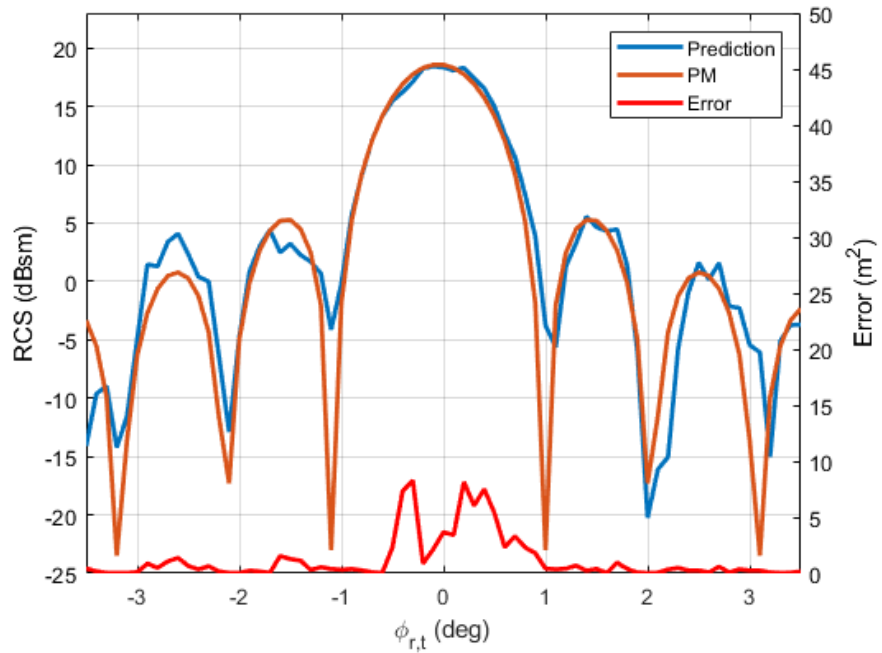


Figure 4.31: Normal scale model prediction results at 35.752 GHz.

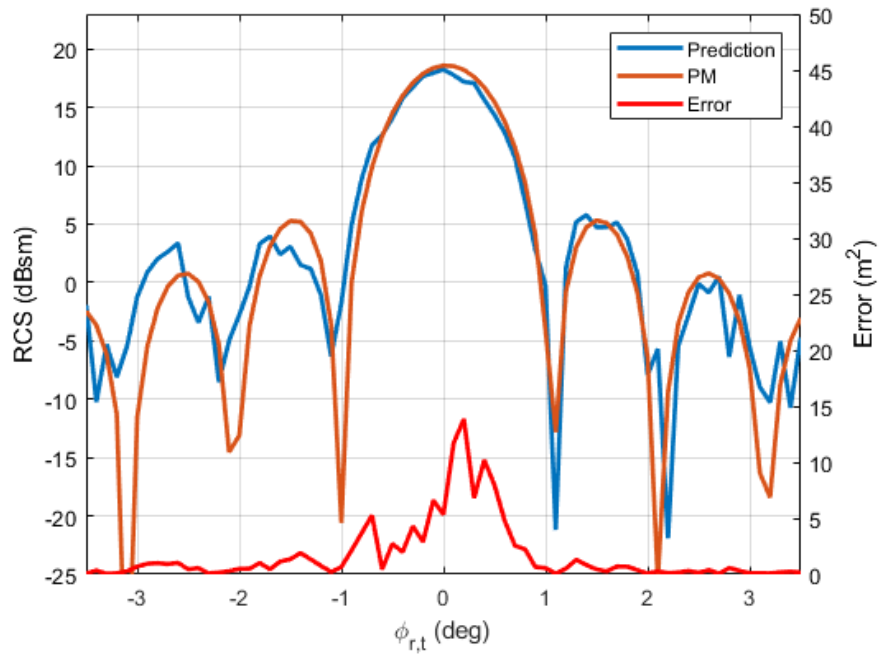


Figure 4.32: Rough scale model prediction results at 35.752 GHz.

Similarly to Figures 4.15-4.20, Figures 4.33-4.38 show the error via (3.13) and relative error via (3.14) for each model predictions peak response as a function of frequency. The mean error or mean relative error is plotted as a red dashed line in each figure. It is again seen from the figures that the measurement error varies noticeably with frequency and similar behavior is seen across the frequency range for each model prediction. As discussed in the previously, it is expected that the error of the Ka-band prediction will include the scaled error of the model measurement. In this case, the model prediction error has a similar pattern to the model measurement error as expected.

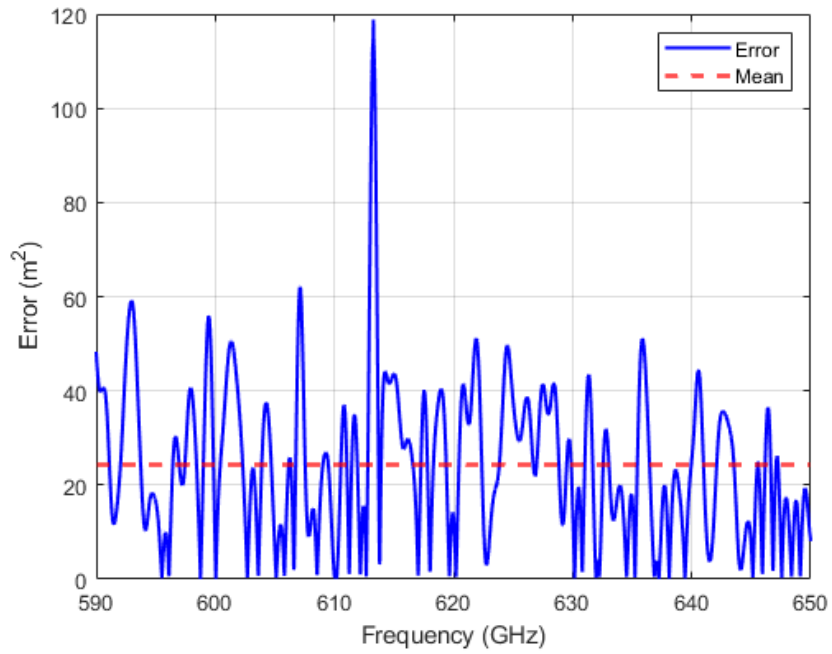


Figure 4.33: Polished scale model prediction error.

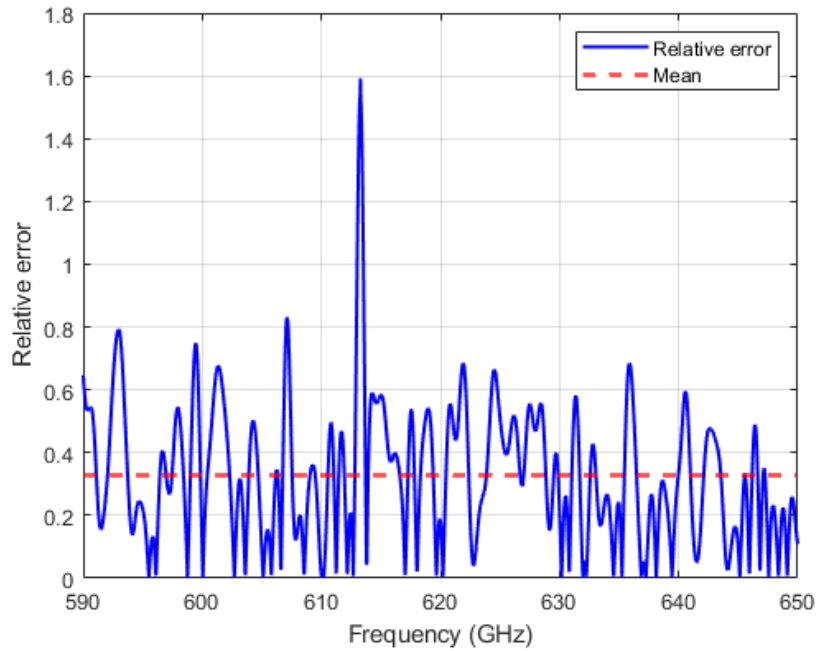


Figure 4.34: Polished scale model prediction relative error.

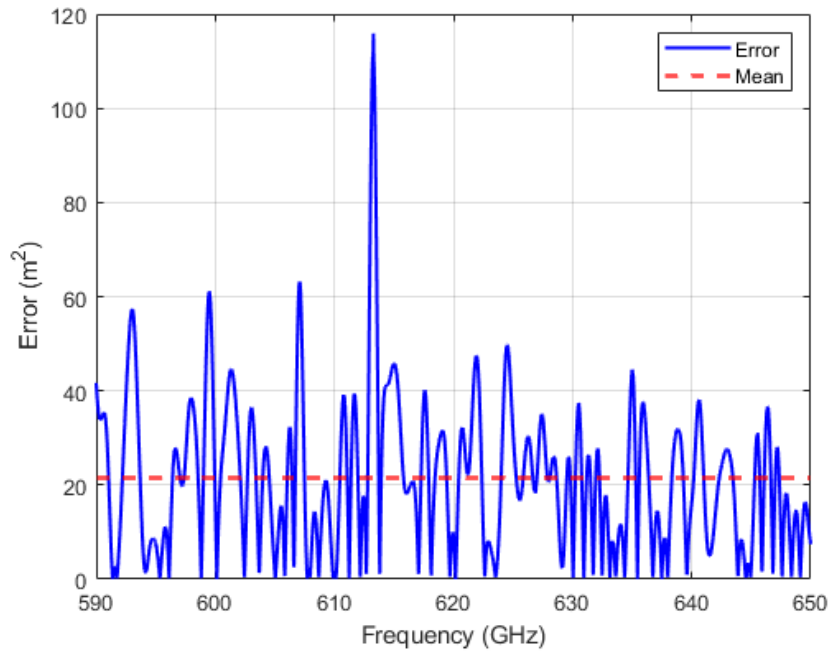


Figure 4.35: Machined scale model prediction error.

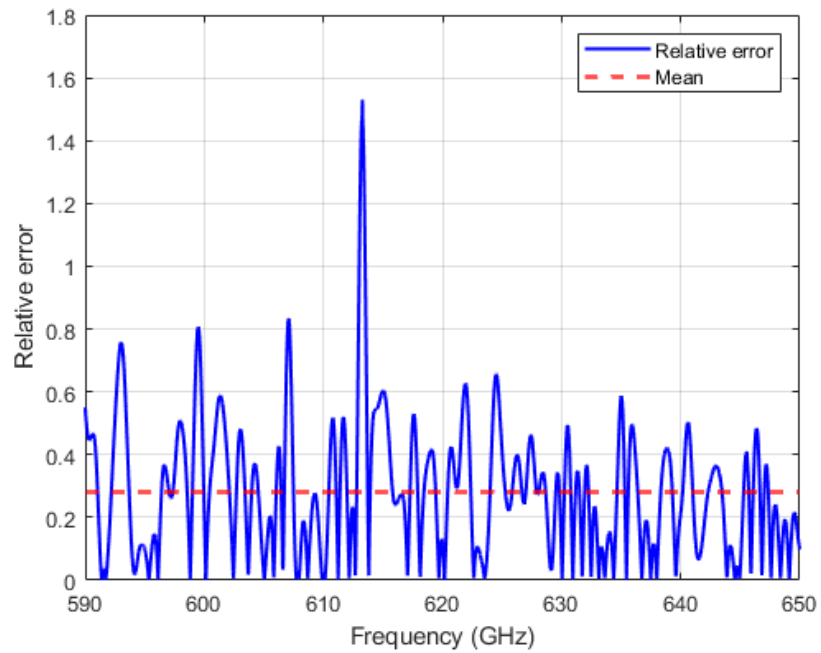


Figure 4.36: Machined scale model prediction relative error.

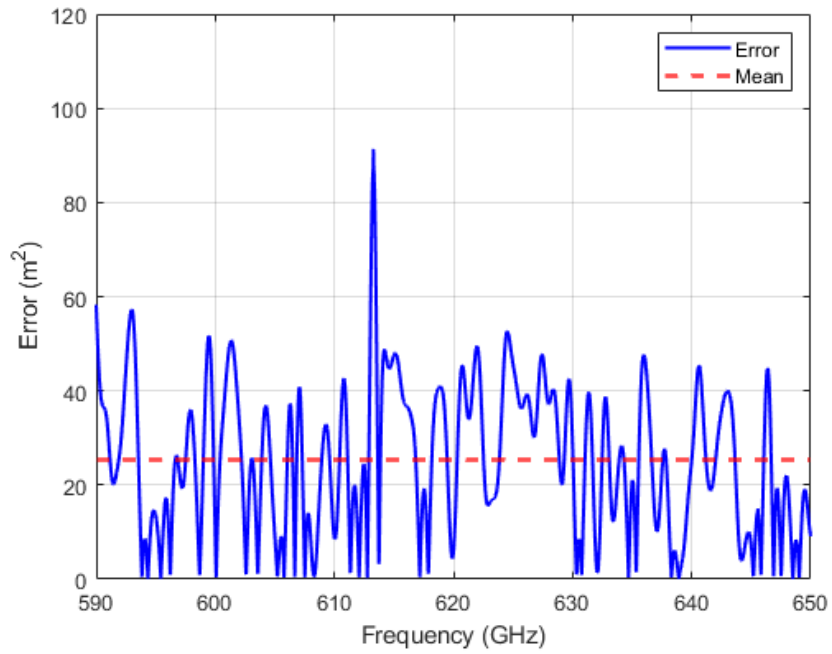


Figure 4.37: Rough scale model prediction error.

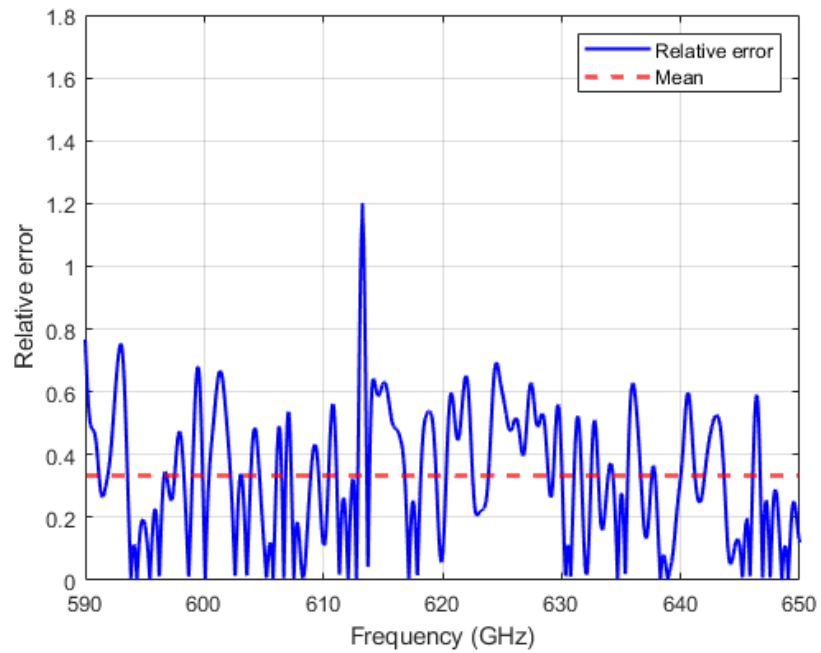


Figure 4.38: Rough scale model prediction relative error.

Table 4.3 lists the mean error and mean relative error over the entire frequency range

measured for each scale model Ka-band prediction. The maximum error is 25.396 m² and the maximum relative error is 0.334. The rough model prediction has the smallest mean relative error across the frequency range, followed by the polished model prediction and then the machined model prediction. The mean relative error has a range of 0.051 between the model predictions.

Table 4.3: Error Between Prediction and PM

Sample	Error (m ²)	Relative Error
Polished	24.439	0.327
Machined	25.396	0.334
Rough	21.460	0.283

4.6 Comparison of Scale Model Prediction to Ka-band Measurement

Figures 4.39-4.44 show the results of the Ka-band RCS prediction via scale model measurements compared to the measured Ka-band RCS. Equations (3.13) and (3.14) are used with the measured Ka-band results in place of the parametric model. The overlapping frequency range of the Ka-band measurement and the scaled THz measurement is plotted. The scaled THz frequency provides RCS prediction between 32.45-35.75 GHz.

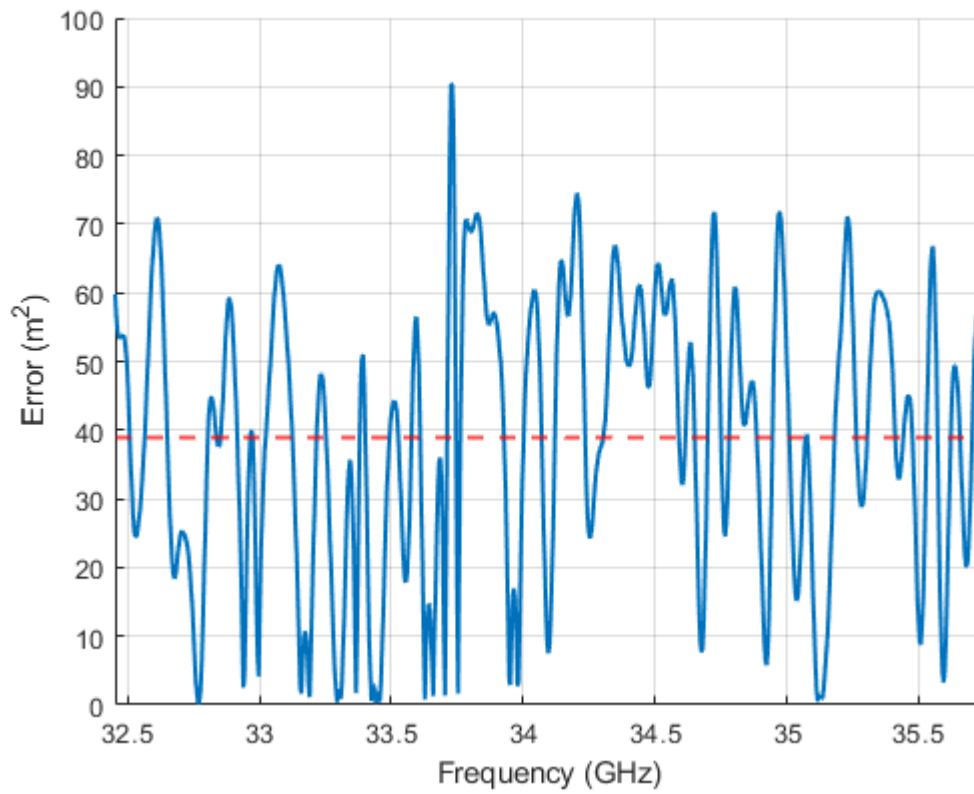


Figure 4.39: Error between polished model prediction and Ka-band measurement.

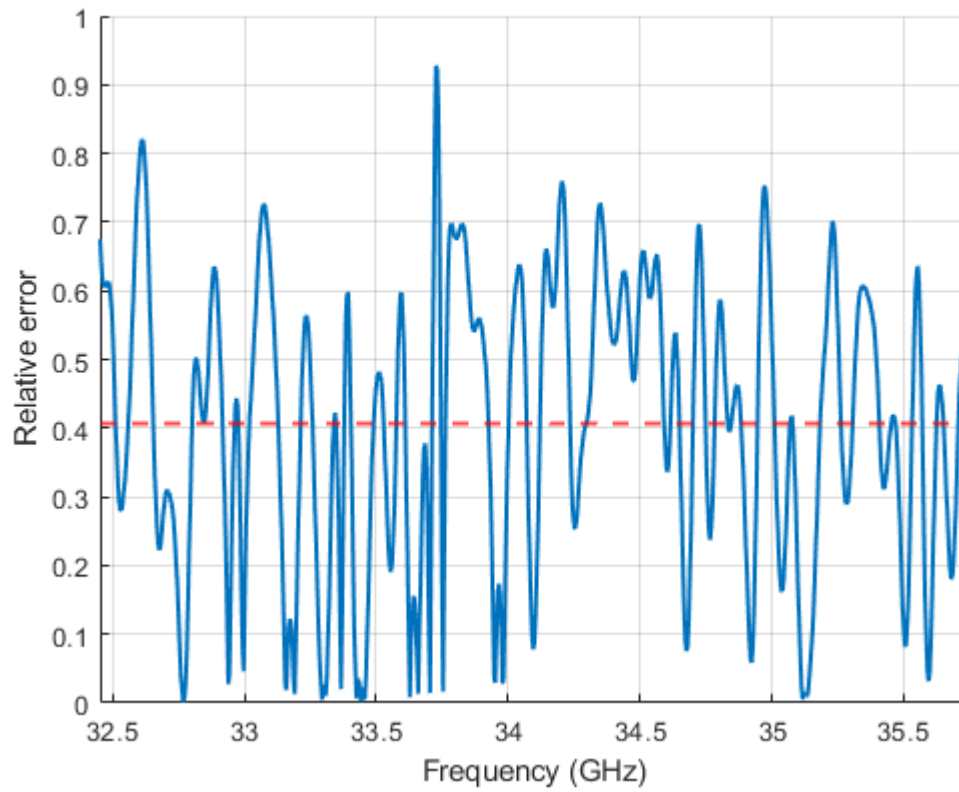


Figure 4.40: Relative error between polished model prediction and Ka-band measurement.

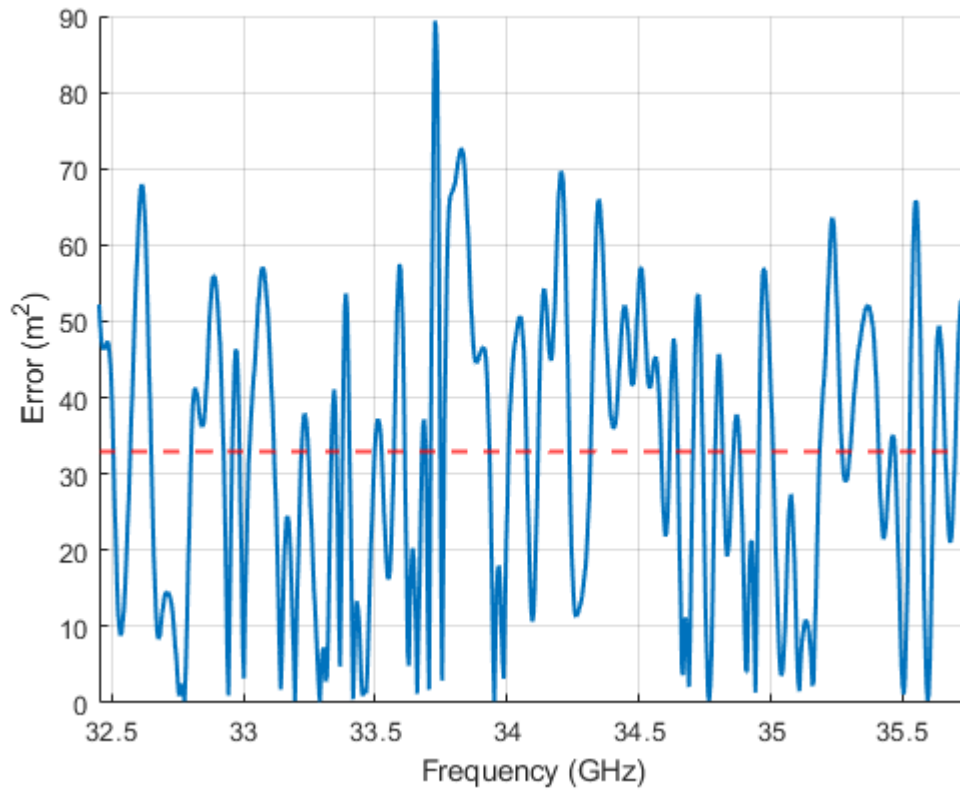


Figure 4.41: Error between machined model prediction and Ka-band measurement.

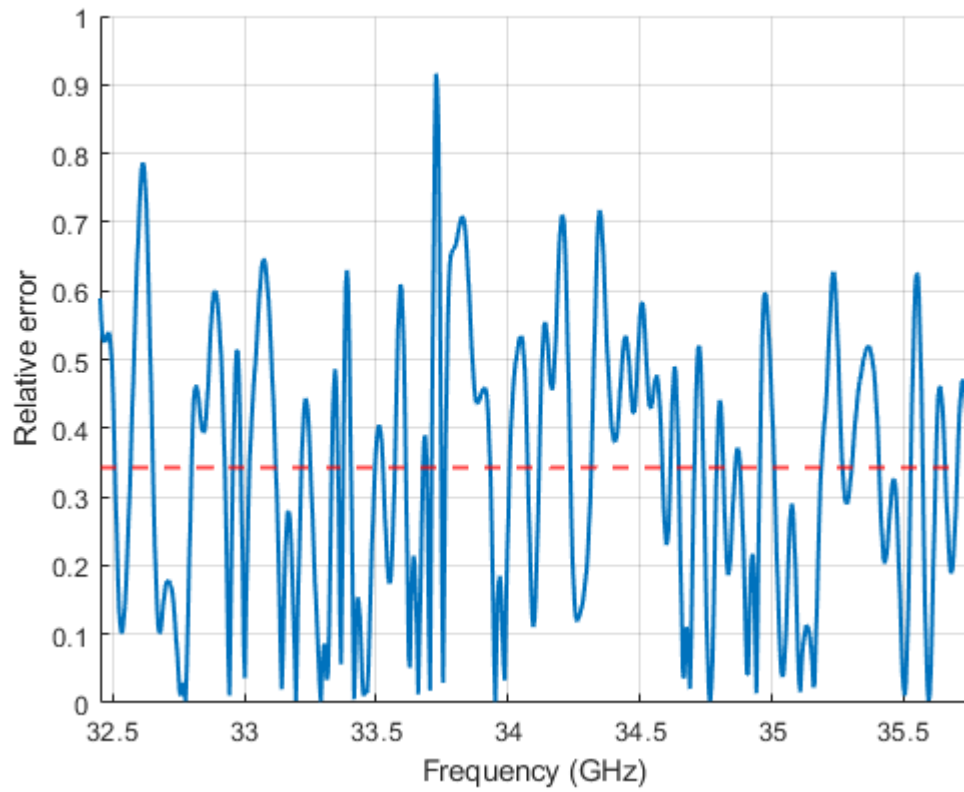


Figure 4.42: Error between machined model prediction and Ka-band measurement.

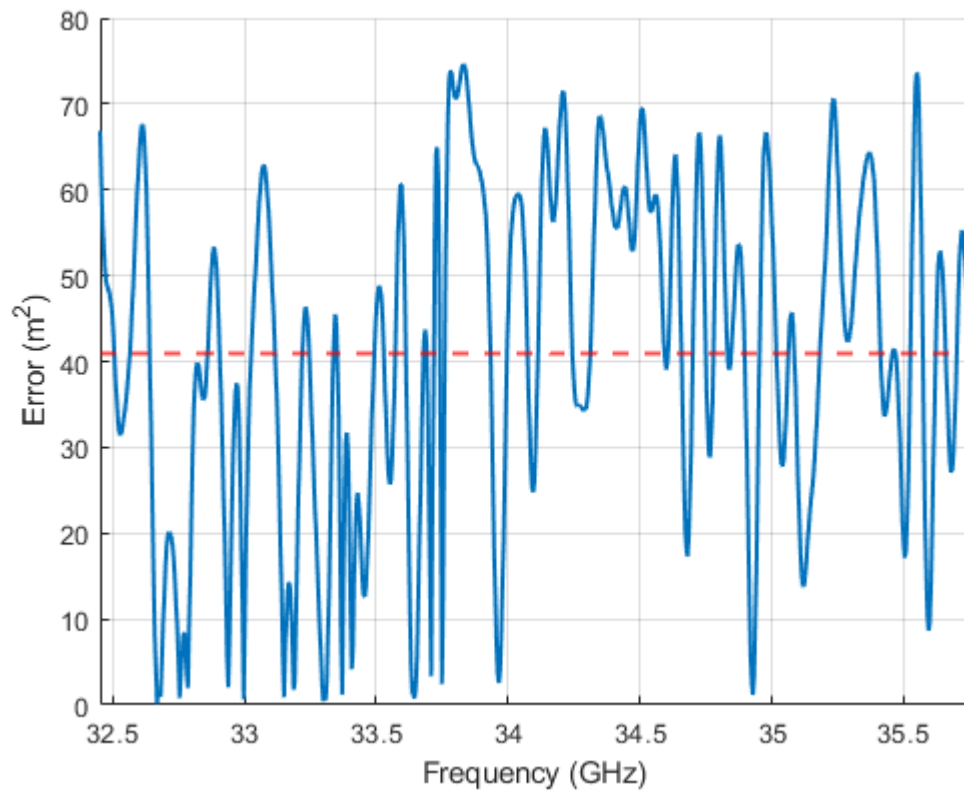


Figure 4.43: Error between rough model prediction and Ka-band measurement.

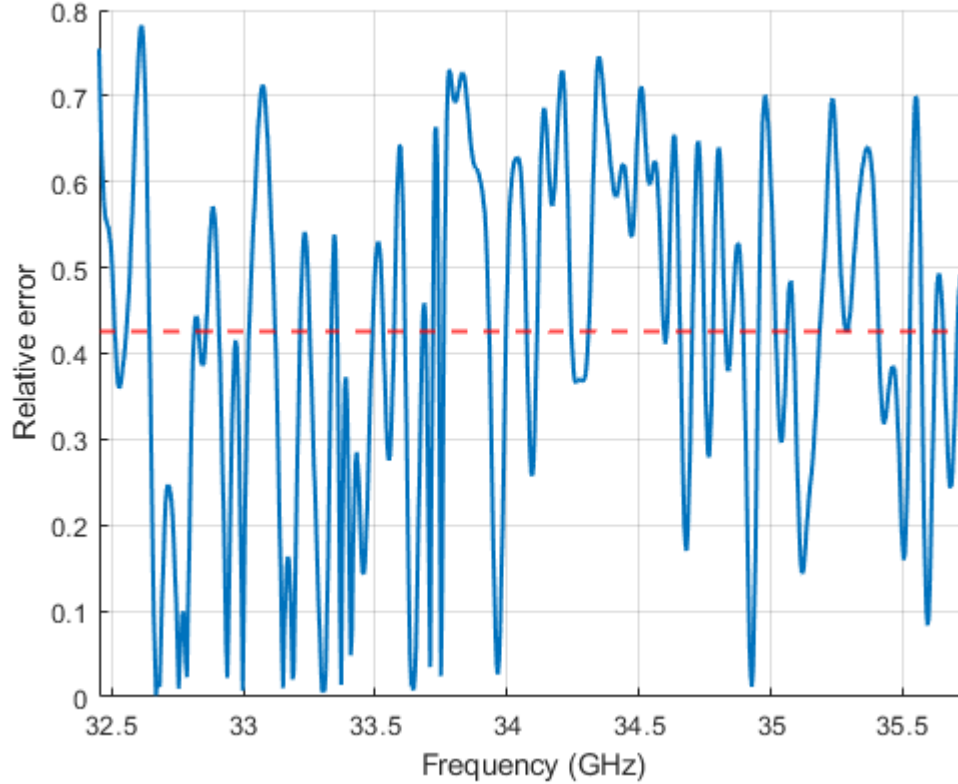


Figure 4.44: Error between rough model prediction and Ka-band measurement.

Table 4.4 lists the mean error and mean relative error between the predicted Ka-band RCS and the measured Ka-band RCS over 32.45-35.75 GHz. This table is important as it demonstrates how well the THz scale models predict the RCS of the Ka-band target in this experiment. It is seen in the table that the relative prediction error varied from 0.343 to 0.426. The machined model has the best agreement with the full-size measurement, followed by the polished model and then the rough model.

Table 4.4: Error Between Prediction and Measurement

Sample	Error (m ²)	Relative Error
Polished	38.923	0.406
Machined	32.835	0.343
Rough	40.993	0.426

Conclusion

5.1 Summary

In this paper, a brief summary of research in the areas of THz imaging, THz scattering from rough surfaces, and scale model measurements is presented. A new 600 GHz coherent laboratory imaging system is described and initial measurements are presented which demonstrate capabilities of the system for RCS measurements and ISAR imaging.

An experiment is developed and executed to investigate the effects of varying surface roughness of aluminium dihedrals on the received bistatic scattering. The RCS of three dihedrals of differing surface roughness (polished, machined, bead blasted) is measured over a determined set of aspect angles. The peak mainlobe specular responses are compared to an accurate parametric scattering model to determine the error of the measurements, and to each other to compare the effects of the varying surface roughness.

The THz model RCS measurements do not have a uniform error over the measurement frequency range and have a similar pattern between the three models. The mean relative error over the frequency range varies from 0.284 for the machined model to 0.328 for the rough model (Table 4.2).

The Ka-band dihedral measurement produced unexpected behavior where the side-lobes were stronger than expected and nulls more shallow than expected. This behavior is likely due to the dihedral not being placed at a far enough range from the system to be in its far field.

The THz scale model targets are used to predict the RCS of the Ka-band target with mean relative error over the measurement frequency range of 0.406, 0.343, and 0.426 for the polished, machined, and rough models, respectively (Table 4.4).

Upon reviewing the relationship between model surface roughness and relative error, there is not a clear distinction. When comparing the predicted Ka-band RCS to the parametric model the roughest surface actually has the lowest relative error. When comparing the predicted Ka-band RCS to the measured RCS the roughest model has the highest relative error. In all cases the maximum variation of the relative error between the differing surface roughness is a maximum of 0.083. In some cases the roughest surface has the highest relative error and in some cases the lowest.

The hypothesis that the roughest surface should have the highest error, followed by targets of descending roughness, was not observed. It would be of interest to perform more experiments with even rougher surfaces to see if a rougher surface is required to produce a clear difference between the model prediction errors. Since the surface roughness of all of the models was much smaller than a wavelength, the surfaces are likely not rough enough to produce the expected results. More study of the measurement system accuracy would provide increased confidence that the system is capable of accurately measuring the expected results. In this paper, it was not demonstrated that the rougher, bead blasted dihedral clearly produced predictions with higher error than the less rough models.

5.2 Recommendations for future work

A thorough study of the accuracy of the measurement system should be completed. This will provide an understanding of what error the system has and what targets can therefore be accurately measured and to what degree the results be trustworthy.

More experiments should be performed with rougher surfaces than those used in this paper. The degree of roughness variation used in this paper may not be enough to produce

an observable or measurable difference in the RCS prediction/measurements with this system.

An area for future work is that of demonstrating the accuracy of THz scale model predictions of more complex targets. This includes the geometric complexity as well as the material complexity. This work used simple dihedrals which are easy to manufacture, offer strong scattering, and have a straightforward parametric scattering model. Real life targets of interest may have much more complicated geometry and be much more challenging to create scale models of.

In addition, in this work highly conductive aluminium targets were used. It is likely that many targets of interest will not be as such, but be comprised of multiple materials. Targets of interest may have heterogeneous material properties, multiple layers or coatings, and even frequency selective surfaces or low observable technology. These warrant a more robust investigation of the limitations of scattering prediction via scale model targets. Two specific limitations are those of the accurate feature recreation in scale models and the accuracy of electromagnetic wave interaction of scale models for frequency dependant materials.

The development of this THz measurement system also provides the opportunity to expand the knowledge of the electromagnetic properties of materials from 500-750 GHz. For example, the extraction of complex permittivity and permeability of materials at these frequencies.

Bibliography

- [1] T. C. Bowman, M. El-Shenawee, and L. K. Campbell, “Terahertz imaging of excised breast tumor tissue on paraffin sections,” *IEEE Transactions on Antennas and Propagation*, vol. 63, no. 5, pp. 2088–2097, 2015.
- [2] T. Ikari, Y. Sasaki, and C. Otani, “Development of terahertz walk-through body scanner using 300 ghz fmcw radar,” in *2022 47th International Conference on Infrared, Millimeter and Terahertz Waves (IRMMW-THz)*, 2022, pp. 1–4.
- [3] H. O. Everitt, W. D. Caraway, and J. T. Richard, “Terahertz (thz) radar: A solution for degraded visibility environments (dve),” U.S. Army Research, Development, and Engineering Command, Redstone Arsenal, United States, Tech. Rep., 2016.
- [4] M. Coulombe, J. Waldman, R. Giles, A. Gatesman, T. Goyette, and W. Nixon, “Submillimeter-wave polarimetric compact ranges for scale-model radar measurements,” in *2002 IEEE MTT-S International Microwave Symposium Digest (Cat. No.02CH37278)*, vol. 3, 2002, pp. 1583–1586 vol.3.
- [5] F. Sheikh, I. B. Mabrouk, A. Alomainy, Q. H. Abbasi, and T. Kaiser, “Indoor material properties extraction from scattering parameters at frequencies from 750 ghz to 1.1 thz,” in *2019 IEEE MTT-S International Microwave Workshop Series on Advanced Materials and Processes for RF and THz Applications (IMWS-AMP)*, 2019, pp. 28–30.

- [6] M. J. Coulombe, T. Ferdinand, T. Horgan, R. H. Giles, and J. Waldman, "A 585 ghz compact range for scale model rcs measurements," in *Proceedings for the Antenna Measurements and Techniques Association*, 1993.
- [7] T. M. Goyette, J. C. Dickinson, J. Waldman, and W. E. Nixon, "1.56-THz compact radar range for W-band imagery of scale-model tactical targets," in *Algorithms for Synthetic Aperture Radar Imagery VII*, E. G. Zelnio, Ed., vol. 4053, International Society for Optics and Photonics. SPIE, 2000, pp. 615 – 622. [Online]. Available: <https://doi.org/10.1117/12.396372>
- [8] K. Linden, W. Neal, J. Waldman, A. Gatesman, and A. Danylov, "Terahertz laser based standoff imaging system," in *34th Applied Imagery and Pattern Recognition Workshop (AIPR'05)*, 2005, pp. 8 pp.–14.
- [9] C. J. Beaudoin, T. Horgan, G. DeMartinis, M. J. Coulombe, T. Goyette, A. J. Gatesman, and W. E. Nixon, "A prototype fully polarimetric 160-GHz bistatic ISAR compact radar range," in *Radar Sensor Technology XXI*, K. I. Ranney and A. Doerry, Eds., vol. 10188, International Society for Optics and Photonics. SPIE, 2017, p. 101880Z. [Online]. Available: <https://doi.org/10.1117/12.2262372>
- [10] G. B. DeMartinis, B. W. Soper, J. D. Cook, T. M. Horgan, L. F. Horgan, C. J. Beaudoin, J. C. Dickinson, and A. J. Gatesman, "A 243 ghz direct-conversion fmcw transceiver for radar moving target signature measurements," in *2018 USNC-URSI Radio Science Meeting (Joint with AP-S Symposium)*, 2018, pp. 13–14.
- [11] J. C. Dickinson, T. M. Goyette, and J. Waldman, "High resolution imaging using 325 ghz and 1.5 thz transceivers," in *15th International Symposium on Space Terahertz Technology*, 2004.

- [12] K. B. Cooper, R. J. Dengler, G. Chattopadhyay, E. Schlecht, J. Gill, A. Skalare, I. Mehdi, and P. H. Siegel, "A high-resolution imaging radar at 580 ghz," *IEEE Microwave and Wireless Components Letters*, vol. 18, no. 1, pp. 64–66, 2008.
- [13] R. J. Dengler, F. Maiwald, and P. H. Siegel, "A compact 600 ghz electronically tunable vector measurement system for submillimeter wave imaging," in *2006 IEEE MTT-S International Microwave Symposium Digest*, 2006, pp. 1923–1926.
- [14] R. J. Dengler, K. B. Cooper, G. Chattopadhyay, I. Mehdi, E. Schlecht, A. Skalare, C. Chen, and P. H. Siegel, "600 ghz imaging radar with 2 cm range resolution," in *2007 IEEE/MTT-S International Microwave Symposium*, 2007, pp. 1371–1374.
- [15] K. B. Cooper, R. J. Dengler, N. Llombart, B. Thomas, G. Chattopadhyay, and P. H. Siegel, "Thz imaging radar for standoff personnel screening," *IEEE Transactions on Terahertz Science and Technology*, vol. 1, no. 1, pp. 169–182, 2011.
- [16] A. Mostajeran, S. M. Naghavi, M. Emadi, S. Samala, B. P. Ginsburg, M. Aseeri, and E. Afshari, "A high-resolution 220-ghz ultra-wideband fully integrated isar imaging system," *IEEE Transactions on Microwave Theory and Techniques*, vol. 67, no. 1, pp. 429–442, 2019.
- [17] A. Huebner, M. A. Saville, E. R. Brown, and P. Sotirelis, "A laboratory imaging system at 600 ghz," in *2022 IEEE Research and Applications of Photonics in Defense Conference (RAPID)*, 2022, pp. 1–2.
- [18] H. Elayan, O. Amin, B. Shihada, R. M. Shubair, and M.-S. Alouini, "Terahertz band: The last piece of rf spectrum puzzle for communication systems," *IEEE Open Journal of the Communications Society*, vol. 1, pp. 1–32, 2020.
- [19] J. Kokkonen, V. Petrov, D. Moltchanov, J. Lehtomaeki, Y. Koucheryavy, and M. Juntti, "Wideband terahertz band reflection and diffuse scattering measurements

- for beyond 5g indoor wireless networks,” in *European Wireless 2016; 22th European Wireless Conference*, 2016, pp. 1–6.
- [20] M. Alissa, B. Friederich, K. Kolpatzeck, A. Czyliwik, and T. Kaiser, “Experimental investigation of terahertz wave scattering by statistically controlled rough surfaces,” in *2019 IEEE MTT-S International Microwave Workshop Series on Advanced Materials and Processes for RF and THz Applications (IMWS-AMP)*, 2019, pp. 100–102.
- [21] E. F. Knott, *Radar Cross Section Measurements*. SciTech Publishing, 2006.
- [22] Y. Zhang, A. Huston, R. D. Palmer, R. Albertson, F. Kong, and S. Wang, “Using scaled models for wind turbine em scattering characterization: Techniques and experiments,” *IEEE Transactions on Instrumentation and Measurement*, vol. 60, no. 4, pp. 1298–1306, 2011.
- [23] M. A. Saville, P. Sotirelis, J. D. Compaleo, and H. L. Judd, “Designing empirical lab experiments for sar-atr,” in *2018 IEEE Research and Applications of Photonics In Defense Conference (RAPID)*, 2018, pp. 1–4.
- [24] M. A. Saville, J. D. Compaleo, H. L. Judd, J. Smith, and P. Sotirelis, “Designing isar lab experiments for eo-sar atr,” *IEEE Photonics Journal*, vol. 11, no. 3, pp. 1–10, 2019.
- [25] M. J. Campbell, J. P. Smith, N. Miller, and M. A. Saville, “Improvement of continuous-wave radar measurements in a partially controlled environment,” in *2016 IEEE Conference on Antenna Measurements & Applications (CAMA)*, 2016, pp. 1–4.
- [26] Keysight Technologies. N5224a pna microwave network analyzer, 43.5 ghz. [Online]. Available: <https://www.keysight.com/us/en/product/N5224A/pna-microwave-network-analyzer-435-ghz.html>

- [27] Virginia Diodes, Inc. Vector network analyzer extenders. [Online]. Available: <https://www.vadiodes.com/en/products/vector-network-analyzer-extension-modules>
- [28] Mini-Circuits. Zkl-1r5 coaxial amplifier. [Online]. Available: <https://www.minicircuits.com/pdfs/ZKL-1R5.pdf>
- [29] Newport Corporation. Motion controller, esp301, 3-axis, usb,rs232. [Online]. Available: <https://www.newport.com/p/ESP301-3N>
- [30] ——. Urs-b series rotation stage user's manual. [Online]. Available: https://www.newport.com/medias/sys_master/images/images/hb2/hea/9131988516894/URS-B-User-s-Manual.pdf
- [31] Thomas Keating Ltd. Corrugated horns. [Online]. Available: <http://www.terahertz.co.uk/tk-instruments/products/corrugatedhorns>
- [32] Virginia Diodes, Inc., *VNA Extension Modules Operational Manual*, 2022.
- [33] Keysight Technologies, *PNA Family Microwave Network Analyzers Configuration Guide*, 2014.
- [34] “Ieee recommended practice for radar cross-section test procedures,” *IEEE Std 1502-2020 (Revision of IEEE Std 1502-2007)*, pp. 1–78, 2020.
- [35] D. L. Mensa, *High resolution radar cross-section imaging.*, ser. The Artech House radar library. Artech House, 1991.
- [36] Mitutoyo America Corporation. Quick guide to surface roughness measurement. [Online]. Available: https://www.mitutoyo.com/webfoo/wp-content/uploads/1984_Surf_Roughness_PG.pdf
- [37] J. A. Jackson, B. D. Rigling, and R. L. Moses, “Parametric scattering models for bistatic synthetic aperture radar,” in *2008 IEEE Radar Conference*, 2008, pp. 1–5.

- [38] A. Tempelis, M. Jussaume, and J. A. Jackson, “Comparison of measured and predicted bistatic scattering from a right-angle dihedral,” in *2011 IEEE RadarCon (RADAR)*, 2011, pp. 135–140.